Fabrication and Characterization of TiO_2-PMMA Composite Fibers for Photocatalytic Environmental Remediation

by

Namrata Kanth

A Thesis Presented in Partial Fulfillment for the Degree
Master of Science

Approved by the
Graduate Committee:

Kenan Song, Co-Chair
Sefaattin Tongay, Co-Chair
Arunachala Mada Kannan

ARIZONA STATE UNIVERSITY

May 2020

ABSTRACT

Photocatalytic activity of titanium dioxide (titania or TiO_2) offers enormous potential in solving energy and environmental problems. Immobilization of titania nanoparticles on inert substrates is an effective way of utilizing its photocatalytic activity since nanoparticles enable high mass-transport, and immobilization avoids post-treatment separation. For competitive photocatalytic performance, the morphology of the substrate can be engineered to enhance mass-transport and light accessibility. In this work, two types of fiber architectures (i.e., dispersed polymer/titania phase or D-phase, and multi-phase polymer-core/composite-shell fibers or M-phase) were explored as effective substrate solutions for anchoring titania. These fibers were fabricated using a low-cost and scalable fiber spinning technique. Polymethyl methacrylate (PMMA) was selected as the substrate material due to its ultraviolet (UV) transparency and stability against oxidative radicals. The work systematically investigates the influence of the fiber porosity on mass-transport and UV light scattering. The properties of the fabricated fiber systems were characterized by scanning electron microscopy (SEM), Brunauer–Emmett–Teller (BET), UV-vis spectrophotometry (UV-vis), and mechanical analysis. The photocatalytic performance was characterized by monitoring the decomposition of methylene blue (MB) under UV (i.e., 365 nm) light. Fabrication of photocatalytic support structures was observed to be an optimization problem where porosity improved mass transport but reduced UV accessibility. The D-phase fibers demonstrated the highest MB degradation rate (i.e., 0.116 min^{-1}) due to high porosity (i.e., 33.2 m^2/g). The M-phase fibers reported a better degradation rate compared to a D-phase fibers due to higher UV accessibility efficiency.

DEDICATION

To my dear husband, whose relentless support and vibrant presence have made my life wonderful

Also to my family and friends, for the meaningful experiences that have shaped my personality and career choices

ACKNOWLEDGMENT

I would like to first thank my advisor, Dr. Kenan Song, for advising me for the past 1.5 years. For always sparing time and being extremely approachable. I will certainly hold on to the problem-solving techniques I learned while working in the lab and apply it during my future endeavors. I would also like to thank all my lab mates Weiheng Xu, Rahul Franklin, Dharnidar Ravichandran, and Sayli Jambhulkar, whom I now consider as dear friends. Their presence struck a perfect balance between social life and research. I would also like to give many special thanks to Weiheng Xu for thoroughly reviewing my work, providing critical insights, and conducting countless experimental trials. Also, appreciation will be given to Dharnidar Ravichandran for helping with multiple experiments.

Last but not least, I would also like to thank Dr. Tongay and Dr. Kannan, for serving as my committee members. Dr. Tongay's class (i.e., MSE 598) was one of the best courses I have attended so far. Those lessons made me appreciate the intricacies of photocatalysis. Thanks are given to Dr. Kannan for allowing the use of the UV-vis equipment. Also, I would like to extend my thanks to Umesh Prasad (Dr. Kannan's student) for sharing his knowledge about photocatalysis.

TABLE OF CONTENTS

Page

LIST OF TABLES

Table Page

LIST OF FIGURES

Figure Page

Figure Page

Figure Page

ABBREVIATIONS

Characterizations:

BET	Brunauer, Emmett and Teller
DSC	Differential Scanning Calorimetry
EDS	Electron Dispersive Spectroscopy
SEM	Scanning Electron Microscopy
TGA	Thermogravimetric analysis
UV-vis	Ultraviolet-visible spectrophotometry

Sample Materials:

CS_M	M-phase fiber sample
D-phase	single phase porous PMMA-titania fiber
D_5	D-phase fiber of diameter = 0.5 mm
D_{10}	D-phase fiber of diameter = 1.0 mm
M-phase	Multiphase fiber with PMMA core and porous PMMA-titania shell
S-phase	Single-phase PMMA fiber
S_M	S-phase melt-spun fiber
S_S	S-phase solution spun fiber

Solvent Materials:

DMAc	Dimethylacetamide
THF	Tetrahydrofuran

Polymer Materials:

PAN	Polyacrylonitrile
PC	Polycarbonate
PDMS	Polydimethylsiloxane
PEG	Polyethylene glycol
PET	Polyethylene terephthalate
PMMA	Polymethyl methacrylate
PMMA-1	PMMA films prepared by casting
PMMA-2	porous PMMA film prepared by phase inversion
PMMA-3	porous PMMA films prepared by phase inversion including titania nanoparticles. (PMMA:TiO_2 weight ratio of 2:1)
PP	Polypropylene
PS	Polystyrene
PTFE	Polytetrafluoroethylene
PVA	Polyvinyl alcohol
PVC	Polyvinyl chloride
PVDF	Polyvinylidene difluoride
Tween-80	Polysorbate 80

Titania	Titanium dioxide or TiO_2

SYMBOLS

α	Absorbance
C	MB concentration (mg/L)
C_0	Initial MB concentration (mg/L)
E_g	Semiconductor band gap, eV
k	Degradation rate (min^{-1})
R	Reflectance, %
t	Time in minutes
T	Transmittance, %

CHAPTER 1.

THESIS SYNOPSIS

Polymer-based fibers have a broad range of applications such as light transmittance, drug delivery[1], sensors[2], wastewater filtration[3] and disinfection[4], and additive manufacturing[5], to name a few. Polymer fibers are usually ductile plastics, and incorporating reinforcement phases can enhance their mechanical and functional properties[6]. These reinforcement phases include nanoscale carbons that can improve the elastic modulus or fracture strength[7,8], metals that can incorporate conductivity and permeability[9], and ceramic or glass nanofillers to induce thermal dissipation, optical reflection, and many other smart behaviors[10]. However, the inclusion of these reinforcement fillers and manipulation of their orders has been challenging in fiber spinning. Thus, this thesis will study different manufacturing techniques for composite fibers with separated phases and complex microstructures. The fibers composed of polymethylmethacrylate (PMMA) with either uniform titania (TiO_2 nanoparticles) dispersions or porous coatings will be the study focus for demonstrating water treatment efficiency.

Why titania? Titania is an indirect bandgap semiconductor (bandgap~ 3 eV or 413 nm), which in the presence of light with energy greater than or equal to its bandgap, produces electron-hole pairs. The electron-hole pair form stable oxidizing and reducing radicals capable of degrading organic contaminants into innocuous carbon dioxide and water[11]. **Figure** 1 depicts the mechanism of electron-hole formation and the overall photocatalysis process. This advanced oxidation capability is favorable for addressing energy and

environmental crisis[12]. For example, titania has been widely used for environmental remediation applications of pollutant capture[13], reformation of hydrocarbon fuels[14], treatment of industrial waste[15], and waste-water disinfection[3]. Despite high surface area and photocatalysis efficiency, titania powder or particles suffer from drawbacks of low light utilization in suspensions and expensive post-treatment separation for reuse.[16] For this reason, titania materials need to be fixed on inert substrates[17], including glass, activated carbon, silica gel, and polymeric materials[18]. Polymers are among the extensively researched photocatalysis supports because they are chemically inert, physically processable, mechanically flexible, and cost-efficient [18].

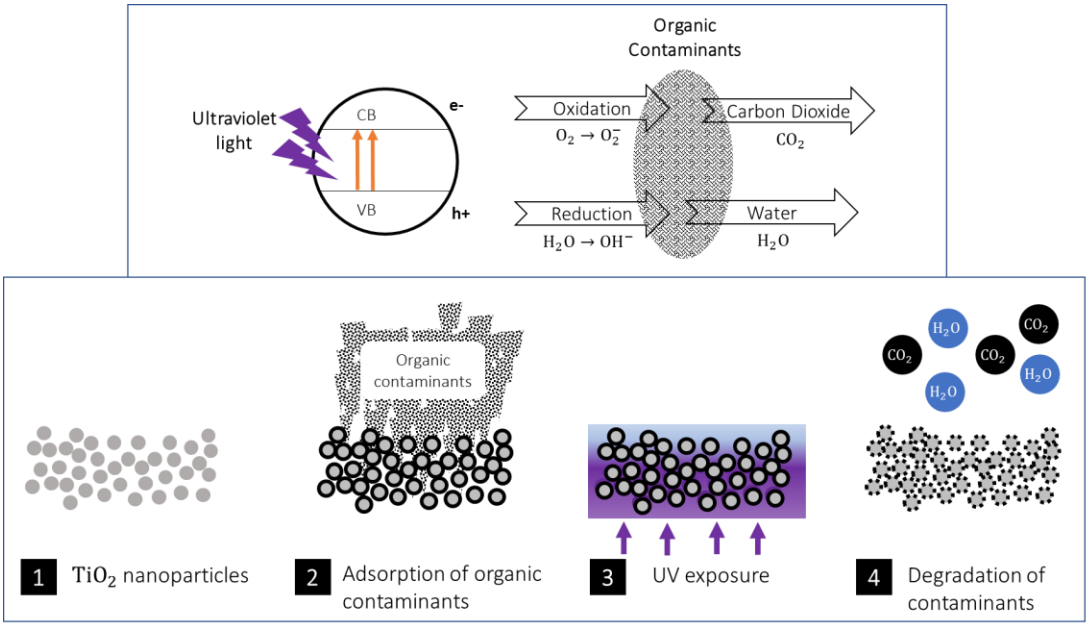

Figure 1. Top Image: Photo-Induced Formation of Electron-Hole Pair in TiO2. Bottom Image: Overall Photocatalysis Reaction Procedure

Why PMMA? Merits of catalyst immobilization come hand in hand with the risk of losing the active catalyst surface by encapsulating titania in the polymer matrix. To

mitigate this risk and improve performance, a high surface to volume ratio is required[19]. Some of the strategies for achieving a high specific surface area is by using porous membranes, mesoporous clays, nanofibers, or nanorods[16]. Another approach was to coat radially emitting optical fibers with titania[20,21]. This unique architecture served two purposes - high surface area by utilizing the fiber longitudinal morphology and remote light accessibility through quartz optical fibers. Among all polymers, PMMA is an excellent candidate to deliver titania due to its suitable optical properties[22] (i.e., UV transparency) and stability against strong oxidative radicals[23], as well as its flexibility in morphology control (e.g., porosity manipulations[24,25]).

Research overview: Given this premise, titania-PMMA composite fibers with well-controlled porous morphologies via fiber-spinning and/or dip-coating processes were explored in this work. The goal of the research was to demonstrate the development of titania-PMMA composite fibers using a low-cost fiber fabrication technique and achieve a photocatalytic performance comparable to or better than the existing system. The objective was to fabricate, characterize, and quantify the photocatalytic performance of these fibers systems. The porous structure was rendered to the titania-PMMA composites by phase inversion using immersion precipitation. First, the structural and optical properties critical of photocatalysis, such as intrinsic features of the titania-PMMA composites (i.e., pore sizes, porosity, and UV accessibility achievable by phase inversion) as a function of processing parameters, were characterized. Second, based on the optimized processing conditions, two fiber architectures were fabricated and studied,

named as D-phase and M-phase fibers. A schematic sketch of the fibers is shown in **Figure** 2. The fiber characteristics are described below,

- The dispersed phase fibers (i.e., D-phase) were the single-phase, porous, PMMA/titania fibers made by the solution-spinning technique. Two D-phase fiber samples of different diameters were analyzed to understand the influence of fiber size on structural properties and its consequential impact on photocatalytic performance.
- The multiphase fibers (i.e., M-phase) were composed of a core-shell structure. The fiber core was a UV-transparent PMMA, and the fiber shell was a porous titania-PMMA composite. The fibers were fabricated in a two-step process. The melt-spinning technique prepared the fiber core, and the dip-coating method coated the shell on fiber surfaces. The M-phase fibers had a superior architecture compared to D-phase fibers[26]. The fiber core was provided for remote UV accessibility, and the porous fiber shell was provided for enhanced sites for photocatalytic adsorption.

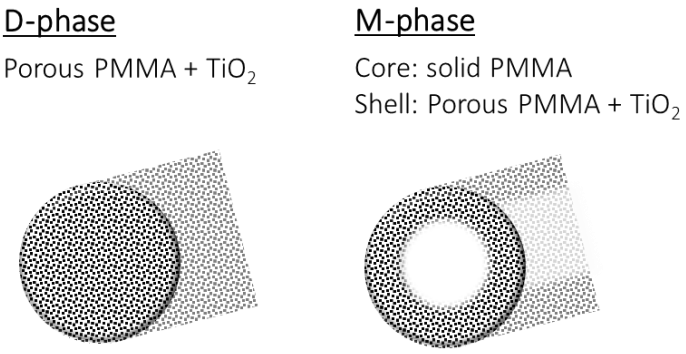

Figure 2 Schematic Sketch of Fiber Samples Analysed in this Study

The structural properties of the fibers were characterized using Scanning Electron Microscopy (SEM), Electron Diffraction Scattering (EDS), and Brunauer, Emmett and Teller (BET) particle analyzer. The photocatalytic performance and reusability of the

fibers were assessed as a function of methylene blue (MB) concentration at different environmental conditions (i.e., UV intensity, time, cycles).

In this thesis, Chapter 2 summarizes the state-of-the-art in fiber spinning with complex fiber morphologies and hierarchical microstructures. Chapter 3 introduces the experimental details, followed by the results and discussions (Chapter 4) and the conclusions/prospects (Chapter 5).

CHAPTER 2.

LITERATURE REVIEW

Understanding of the fabrication procedures is essential since it influences the morphology, structural integrity, and porosity of the fibers. This section will first review polymer fiber spinning techniques, including categories of melt spinning, solution spinning (i.e., wet-spinning, dry-spinning, and gel-spinning or dry-jet wet-spinning), and electrospinning. Then the polymer fiber architectures with complex phase separations are introduced. At last, the porous structures from multiple processing techniques concluded this chapter.

2.1 Fiber Spinning Methods

Polymer fiber spinning involves extruding a moldable polymer melt or polymer solution via a spinneret, followed by solidifying the polymer to retain the desired shape. The structure of the fiber depends on the spinneret design, spinning dope viscosity, and draw ratio, as well as the specific spinning procedures. The viscosity can be controlled by the polymer molecular weight, the concentration in solutions, or the melt temperature. Low viscosity cannot provide enough strength for the fiber to be continuously fabricated due to the weak entanglement among polymer chains. Conversely, high viscosity will clog the spinneret. [27] Depending on the moldability of the polymer and the type of spinning techniques, fibers of dimensions ranging from millimeters to centimeters can be fabricated.

Melt Spinning: The polymer is typically melted above the glass transition and below the degradation temperature to ensure the smooth flow of the polymer through an extruder[28]. The polymer emerging from the spinneret must be either cooled or quenched to retain its geometry. Polymers used for melt spinning should be linear and possess a high enough molecular weight. Linear polymer chains are recommended since the melting process entangles them and makes them pliable for large extensions. The high molecular weight provides high intermolecular forces to stretch the polymer into high aspect ratio fibers.

Solution Spinning: Solution spinning involves dissolving the polymers in a good solvent as the spinning dope is supplied to the extruder for fiber-making. The solvent is eventually removed from the dope by either coagulation (**wet-spinning**[29]) or evaporation (**dry-spinning**) to allow solidification[30]. Wet-spinning will gel fibers in a coagulation bath and dry-spinning will solidify fiber in a heating chamber. It is especially useful for making fibers from high melting temperature polymers or polymers with a melting point above the degradation temperature. Unlike melt spinning, the viscosity of the extruded mixture is much lower, and fibers of much thinner diameter can be fabricated. Variations of the spinning dope or processing conditions can also lead to other relevant spinning methods, for example, the **gel-spinning**[31]**.** Gel-spinning uses high molecular weight polymer dissolved in a solvent, and the high molecular weight gives the solution sufficient viscosity for being drawn into fibers. Since the individual molecular chains are connected well, the polymer fibers exhibit high tensile strength and modulus. This spinning technique is colloquially used for any spinning technique where the dope is

heavily viscous, or the solvent concentration is higher than 40%. Another example will be the **dry-jet wet-spinning**[32], where the solution or the gel will be injected into the air for maximum drawing and elimination of air-bubbles before the coagulation process for fiber formation.

Electrospinning: Electrospinning uses both melts and solutions for nanoscale fibers upon applying an electrical voltage between the injection spinneret and the collection plates. This technique produces nanoscale fibers whose morphology can be controlled by varying the solution viscosity, environmental conditions and applied electric potential[33].

2.2 Polymer Fiber Architectures

A combination of dissimilar materials (e.g., two or more) in a unique fashion is referred to as architectured polymer fibers. Some of the reported configurations are core-shell (C/S), side by side (S/S), or island-in-the-sea (I/S) (**Figure** 3)[26]. Amongst these, the C/S configuration has gained much attention due to manufacturing ease, and its broad applications in areas of drug delivery[34,35], self-healing fibers[36], battery electrodes[37], supercapacitors[38–40], tissue regeneration[41], nano-based electronics[42], and microwave communication[43].

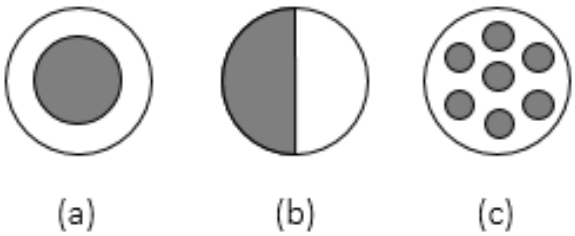

Figure 3. Schematic of Different Bicomponent Fibers (a) CS, (b) S/S, and (c) I/S[26]

Table 1. Summary of spinning techniques

Spinning Technique		Extrusion Temperature	Spinning dope type	Filament Curing Method	Drawing Technique	Viscosity of Dope	Mechanical Strength	Diameter
Melt spinning		Above Tg	Melt	Cooled at room temperature	Automated Winder	Highest	Lack of impurities results in compact fibers with high strength.	Depends on the nozzle size. Ranges from a 50 µm up to a few centimeters.
Solution spinning	Dry-spinning	Below Tg	Solution (preferably volatile)	Stream of hot air or thermally induced solvent removal	Automated winder or collected in pieces (if not strong enough)	High	Solution-based spinning techniques create inherently porous fibers which have lower strength compared to melt-spun fibers	Depends on the viscosity of the dope. Lower viscosity results in a smaller diameter (as small as 50 nm)
	Wet-spinning		Solution (preferably non-volatile)	Immersion precipitation or coagulation		Low		
	Dry-jet-wet-spinning		Solution (volatile or non-volatile)	Partially through immersion precipitation		Intermediate		
Electrospinning			A mixture of volatile and non-volatile solvent	Vapour induced phase separation	The electric charge used to overpower surface tension giving rise to the Taylor cone	Lowest		

2.3 Porous Microstructural Fabrications

Porous structures can increase the overall surface area that provides enhanced sites for adsorption[44], ion trapping[45], filtration[9], and purification[46]. There are numerous ways for fabricating porous polymers with general applications in fibers, membranes, or foams. Some pore-forming techniques include stretching, phase inversion techniques, track etching, electrospinning, polymerization, interfacial sintering.[47] A summary of these fabrication techniques are listed in **Table** 3. SEM images comparing some pore generation techniques is shown in **Figure** 4.

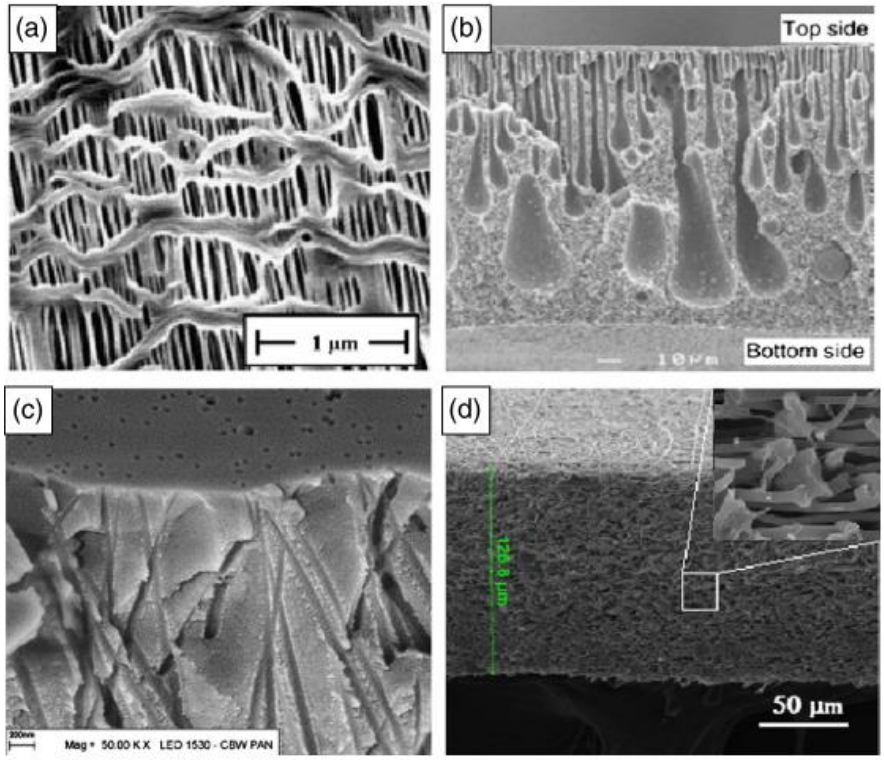

Figure 4. SEM Micrographs for Different Pore Geometries. (a) Cold and Hot Stretching (b) Phase Inversion Technique (c) Track-Etching (d) Electrospinning[47]

Table 2.

Summary of Pore Generation Techniques

Pore Generation Method	**Processing Procedures**	**Pore Sizes (μm)**	**Porosity characteristics**	**Materials**	**Applications**	**Ref.**
Phase Inversion	Demixing of liquids involving a coagulation agent	~0.0001 to 0.01	Higher porosity near the coagulant or non-solvent front, and gradually decreases through thickness of the material	PVDF, PAN, PS, silicone	water distillation and desalination	48,49, 50,51
Solution Casting	Evaporation of volatile solvent leading to solute precipitation	~0.001 - 0.01		polyamide	ultrafilteration	52,53
Interfacial Polymerization	Removal of inert filler post polymerization		Uniform porosity	polyamide	reverse osmosis, ultrafilteration	54,55
Track-etching	Bombarding the surface with ions to create surface pores	~ 0.001 – 0.1	Pore only at the surface	PP, PC, PET	membranes for water purification	56
Electrospinning	Use of electric charge to create fine fibers, cluster of these fibers are used to form porous surfaces		Uniform pores through thickness	PMMA, PDMS, PVC, PVA	drug delivery, tissue engineering	33,57–59
Stretching	Cold stretching to create small fractures on the surfaces, followed by hot stretching to increase the pore size	0.1 - 10	Difficult to control pore size and this process compromises mechanical integrity of structure	PVDF, PTFE, PP	membranes	28,60–62

Abbreviations:

PAN Polyacrylonitrile
PC Polycarbonate
PDMS Polydimethylsiloxane
PEG Polyethylene glycol
PET Polyethylene terephthalate
PMMA Polymethyl methacrylate
PP Polypropylene
PS Polystyrene
PTFE Polytetrafluoroethylene
PVA Polyvinyl alcohol
PVC Polyvinyl chloride
PVDF Polyvinylidene difluoride

2.3.1 Stretching

The stretching technique was developed in the 1970s, and it gained immense popularity due to the simplicity of the process and low cost for being a solvent-free technique.[47] In this technique, the polymer is melt-spun, followed by mechanical stretching it used to create pores. Pore size and orientation can be controlled by varying the extrusion temperature, the viscosity of the melt, and stretching force.[28] This process results in non-uniform pore sizes.

2.3.2 Polymerization

Bulk or interfacial polymerization involves crosslinking the monomer in a cast to create a polymer of the same shape. During the polymerization reaction, the monomer, polymerization initiator, and chain transfer agent filled in a cast will be stimulated by either heat or light.[63,64] For creating a porous structure, an inert filler is dispersed in the monomer mixture, which is leached out during the post-polymerization. The main drawback of this process is the sheer complexity and a need for an expendable mold to build a fiber structure.

2.3.3 Track-etching:

In this technique, a non-porous polymeric structure is bombarded with heavy ions to fracture the surface for pore creation. The duration of irradiation and temperature control the pore size. Track etching is known for precise pore size control ranging from a few

nanometers to tens of micrometers. It is especially recommended for polymers stable towards organic solvents and with good mechanical properties.[47]

2.3.4 Electrospinning:

In this technique, submicron diameter fibers form a highly porous mesh. Precise control of the fiber size, shape, and morphology is used to engineer the desired porosity and pore distribution.[65] The main drawback of this process is that the fiber is not individually collectible and physical manipulation can easily damage it.[47]

2.3.5 Phase Inversion

Phase inversion has gained increased popularity due to easy fabrication procedures, and it produces uniform pores compared to its counterparts. The process involves the use of a polymeric solution which de-mixes into two phases, a polymer-rich phase, and a polymer-lean phase. The de-mixing process is usually driven by heat or interaction with a nonsolvent vapor or liquid. The polymer-rich phase solidifies to form the solid polymeric structure, and the polymer-lean solution is removed, leaving behind a porous morphology[66]. The final morphology of the polymer strongly depends on the properties of the materials and process conditions[67]. The four main techniques of phase separation in polymeric materials are,

- Thermally-induced phase separation

  Solvent quantity decreases by the change in temperature. After demixing is induced, the solvent is removed by evaporation, extraction, or freeze-drying[68].

- Evaporation-induced phase separation

  The polymer is dissolved in a mixture of volatile solvent and a less volatile solvent. During volatile solvent evaporates, leading to precipitation of the polymer. This is similar to the casting process.

- Vapor-induced phase separation

  The polymer solution is exposed to an atmosphere containing a non-solvent. For example, electrospinning of PMMA fibers in a humid atmosphere to leach out solvent producing a highly porous structure[44].

- Immersion precipitation or wet-phase inversion method

  Immersion of polymeric solution is in a nonsolvent bath. Precipitation occurs due to the exchange of solvent in the polymer solution with non-solvent. The solvent and non-solvent must be miscible.

Fibers fabricating by solution spinning process are coagulated on the principle of phase inversion. The final morphology of solution spun fibers is dictated by the rheological properties and solvent-nonsolvent-polymer interaction. During coagulation, the solvent from the fiber diffuses from the extruded filament to the coagulation bath, and the nonsolvent from the coagulation bath diffuses into the fiber. The rate at which the liquid exchange happens decides the final morphology of the fiber. A schematic sketch of phase inversion is as shown in **Figure** 5. There '**S**' represents the solvent, and '**NS**' represents the non-solvent. If the diffusion coefficient of the solvent (D_s) is higher than the diffusion coefficient of the nonsolvent (D_{NS}), then the fiber has a closed formed morphology

without any voids. If the diffusion coefficient of the nonsolvent (D_{NS}) is higher than the diffusion coefficient of the solvent (D_S), then large voids are formed at the fiber surface[69].

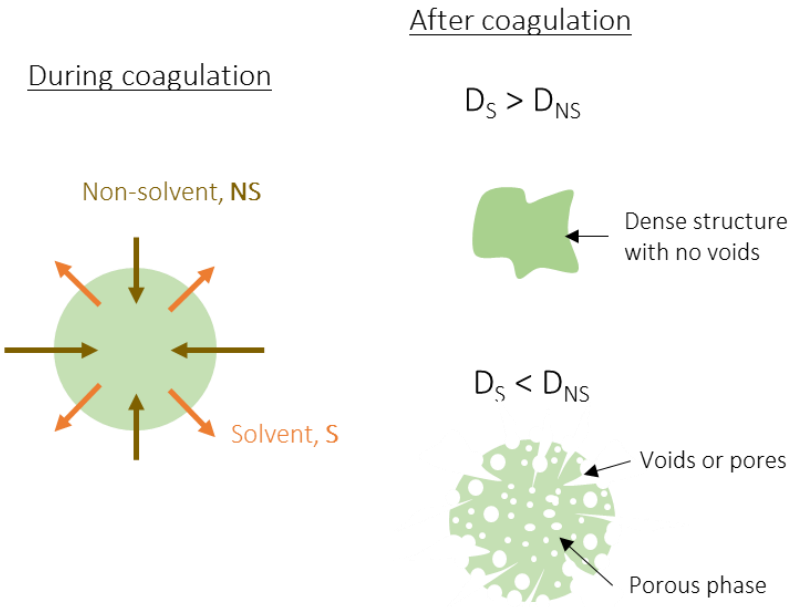

Figure 5. Liquid-Liquid De-Mixing during Solution Spinning[69]

The description above is the simplified version of coagulation physics; it merely defines the extreme states that the fiber morphologies that can be achieved during the coagulation process. To exercise control over the pore size and distribution, a more intricate understanding is required. Termonia et al.[70] elaborately described the fundamentals behind polymer coagulation, and she further classifies the polymer structure as ranging from dust- to finger- to sponge-like morphologies. Termonia et al.[70] emphasized on the importance of solvent/non-solvent coagulant miscibility, which is responsible for initial skin formation that drives the geometry of the coagulated polymer. Similarly, Wang et al.[25] described the influence of coagulant agent using PMMA/acetone 14.5 w/w % solution. PMMA is an amorphous polymer, and the coagulation environment does not

influence polymer crystallization. Surfactants (Tween 80 (hydrophilic nature)) was added to form macro-pores, and three coagulating chemicals were tested, namely water, methanol, and hexane). It was observed that pore size depends on the affinity between solvent and coagulant, as shown in **Figure** 6. Water being the most hydrophilic amongst the three produced highly porous structures. Whereas, hexane being the most hydrophobic, produces the least porous structure.

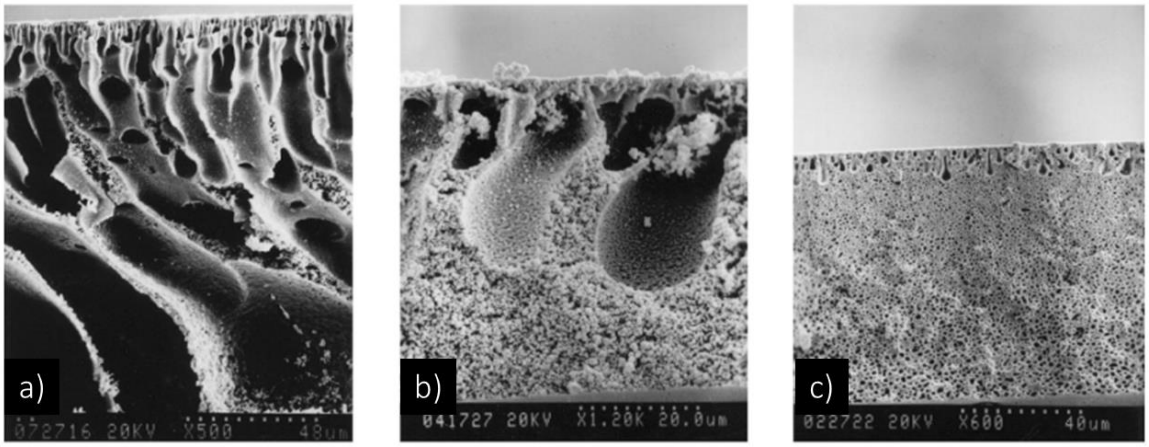

Figure 6. Pore Formation by Addition of 18 vol % of Tween 80 in PMMA/Acetone Solution on Membrane Morphology. Coagulant: a) Water b) Methanol and c) n-Hexane [25]

CHAPTER 3.

EXPERIMENTS

3.1 Chemicals and Materials

Polymethyl methacrylate (PMMA, MW ~120,000), N, N- dimethylacetamide (DMAc), tetrahydrofuran (THF), methanol, hexane, and methylene blue (MB, ≥82% purity) were all obtained from Sigma Aldrich. Titania (TiO_2, P25, ~53 m^2/g) was obtained from Evonik Industries. All polymers and solvents were used as received. Deionized (DI) water was prepared by a Millipore water purification system (Milli-Q Academic).

3.2 Fiber Preparation

Single-phase (S-phase), dispersed-phase (D-phase), and multi-phase (M-phase) fibers were fabricated to understand the influence of fiber morphology on catalysis efficiency. The different fiber structures and their compositional information are listed in **Table** 3. A schematic sketch of the fabrication procedure is shown in **Figure 7**.

- S-phase fibers were fabricated using both melt-spinning and solution-spinning techniques.
    - Melt-spun PMMA fibers (S_M) were prepared using a Noztek Touch screw extruder. PMMA flakes were directly fed into the hopper, and fibers were extruded at 275°C through a 1.4 mm nozzle. Extruded fibers were drawn using an automatic winder to obtain fibers of uniform diameters.
    - Solution-spun PMMA fibers (S_S) were prepared using different combinations of solvents (i.e., DMAc, THF) and coagulants (i.e., DI water, Methanol, and

Hexane) to understand the phase inversion and porosity generations during coagulation procedure. The 25 wt% PMMA/solvent solutions were prepared by magnetically stirrer PMMA flakes with the solvent inside an airtight glass vial to prevent solvent evaporation. The dissolution process took not more than 3 hours at 60°C. The solution was extruded using a syringe through a 1.00 mm diameter nozzle into the coagulant bath.

- D-phase fibers were PMMA-titania composite fibers prepared using the solution spinning technique. In the 25 wt% PMMA/DMAc homogeneous solution (i.e., 25 g PMMA in 100 ml DMAc), 12.5 wt% titania (P25) nanoparticles (i.e., 12.5 g titania) were added. To homogenize the dispersion, it was magnetically stirred at 60°C for an hour inside an airtight glass vial to prevent solvent evaporation. The solution was extruded using a syringe into a DI water coagulation bath. Fiber samples were prepared using nozzles with different diameters of 1.0 mm (D_{10}) and 0.5 mm (D_5).
- M-phase fiber had a core-shell (CS_M) architecture. The core was S-phase (S_M) PMMA fiber. The fiber shell was fabricated by dip-coating the core. The dip-coating solution was a PMMA/TiO_2/DMAc solution (similar to D-phase), and then the coated fibers were immersed in a DI water coagulation bath.

During the coagulation procedure, the fibers were left inside the coagulation bath for 24 hours. The overnight coagulation process ensured that the solvent was effectively leached out during the solvent/non-solvent exchange. The fibers were then dried in an oven maintained at 80°C for 12 hours to ensure complete removal of coagulant from the fiber.

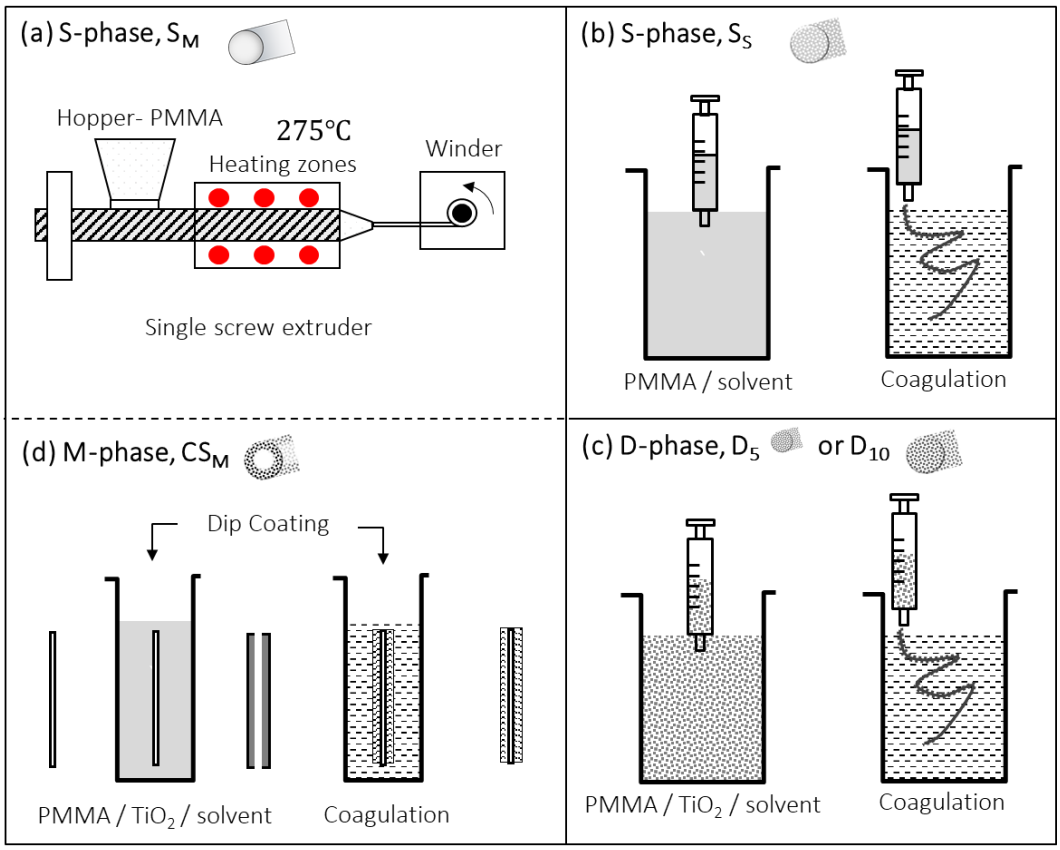

Figure 7 Schematic Sketch of the Fabrication Procedure

Table 3. Different Fibers along With Their Composition and Fabrication Procedure

Fiber Type	Sample Name	Fabrication Method	Fabrication Procedure				
S-phase	S_M	Melt-spinning	As-obtained PMMA extruded in the screw extruder (Noztek) at 275°C temperature through a 1.40 mm diameter				
	S_S	Solution-spinning	In solution spinning, 25 wt% solute (unless otherwise specified) is dissolved in a solvent to form a homogeneous solution. Filler (if specified below) is added to the solution until uniformly dispersed. Following this, the solution is extruded into a coagulation bath using a nozzle with a specified diameter.				
			Solute	**Solvent**	**Filler**	**Coagulant**	**Nozzle Diameter**
D-phase	D_{10}	Solution Spinning	PMMA	DMAc	1:2 wt% titania wrt PMMA weight	Water	1.00 mm
	D_5			DMAc		Water	0.50 mm
M-phase	CS_M	Melt Spinning + Dip coating	The single-phase core (S_M) is dip-coated in the solution (solute: 25%wt PMMA, solvent: DMAc, filler titania 1:2 wt% with respect to PMMA). Dip-coated shell has the same composition as the D-phase fiber.				

3.3 Structural and Optical Property Characterization

The thermal transition of the as-obtained PMMA raw material was studied using thermogravimetric analysis (TGA) (TGA550, TA instruments) and Differential Scanning Calorimetry (DSC) (DSC250, TA Instruments). TGA was conducted in an open environment at a heating rate of 20°C/min. DSC was conducted in a nitrogen environment with a purging rate of 50 mL/min. A heating rate of 10°C/min was used to heat the sample to 278°C (i.e., 0.9 times 308°C, the temperature at which 10% wt PMMA was degraded, per the DSC use standards) and subsequently cooled back to room temperature at 10°C/min.

The morphology of the fibers was observed using a Scanning Electron Microscope (SEM) (XL30 SEM-FEG). Before SEM measurement, all samples were sputter-coated with 15 nm thick gold. Titania retention in the fibers post coagulation was quantified using TGA. The dispersion of Titania across the cross-section of the fibers was observed using Electron Dispersive Spectroscopy (EDS) (XL30 SEM-FEG).

The specific surface area and pore size were measured using BET Surface Area and Porosity Analysis (Tristar II 3020). The bandgap of the as-obtained titania was measured using UV-vis spectrophotometry (UV-vis) (GENESYS 150, Thermo Fisher Scientific). UV-vis was also used to characterize the optical properties of the porous matrix in the D-phase and M-phase fibers. Due to sample size limitations in the UV-vis setup, thin films were fabricated as a representative sample. Even though the complexities in the fabricating films are different from fibers, the results are qualitatively applicable. The

mechanical property of the fibers was characterized by conducting a tensile test using Discovery Hybrid Rheometer (HR-2, TA instruments).

3.4 Photocatalytic Performance Characterization

A back-to-back study was performed to quantify the photocatalytic performance of D-phase and M-phase. Samples containing the same quantity of titania (~50 mg) were prepared. The performance was assessed by studying the degradation kinetics of MB solution (3.2 mg/L). MB is a UV stable dye that degrades in the presence of UV illuminated titania. MB dye has a distinctive blue that vanishes as the dye degrades. The dye concentration was measured by monitoring the absorption peak at 665 nm using a UV-vis spectrophotometer (UV-vis, GENESYS 150, Thermo Fisher Scientific). A 115W 365 nm cross-linker oven was used as a UV radiation source (DYMAX ECE 5000). The degradation of 8 ml MB solution containing 50 mg titania is shown in **Figure** 8. Here, the time in minutes is the amount of time the sample was kept in the UV oven.

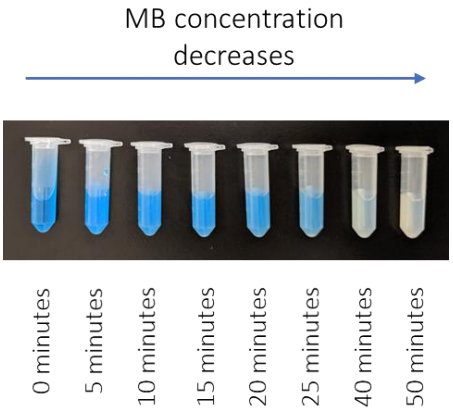

Figure 8 Degradation of Methylene Blue (MB) Solution (3.2 mg/L) in the Presence of UV Illuminated Titania

D-phase samples (i.e., D_5 and D_{10}) weighing 0.15 g (i.e., containing ~50 mg of titania since PMMA: titania = 2:1) were prepared and stored in an 8 mL glass vials. Similarly, M-phase (CS_M) with 0.15 g of shell coating (i.e., containing ~50 mg of Titania since PMMA: titania = 2:1) was collected in another 8 mL glass vial. The shell weight was estimated by calculating the difference between the weight of the coated fiber with the uncoated fiber. The sample vials were put in 8 ml MB solution. Experiments were designed to evaluate the kinetics of MB removal by adsorption and photodegradation. The fibers were first kept in the dark for 5 days to attain adsorption-desorption equilibrium[4,71,72]. Then the samples were exposed to UV radiation until MB decomposed, leaving behind clean and transparent water. The change in MB concentration during UV exposure was recorded in these experiments. The photocatalytic reaction kinetics was analyzed using the Langmuir-Hinshelwood pseudo-first-order kinetics model.[72]

$$\ln\left(\frac{C}{C_o}\right) = -kt$$

Here, C_0 and C represents the dye concentration after the 5-day soaking period and during UV exposure, respectively. k represents the degradation rate and time, t is recorded from the instant when the sample is placed in the UV oven. The parameters C_0 and k are estimated by regression fit using JMP.

The following experiments were designed to study the impact of morphology, porosity, and UV accessibility on photocatalytic performance.

- D-phase samples were studied to understand the influence of porosity on photocatalytic performance. The reusability of the fibers was evaluated by conducting the experiments over two continuous cycles. (#1 and #2)
- M-phase fibers, as compared to D-phase fibers, provided more accessibility by transmitting light through the fiber core.
    - One set of experiments was designed to study the overall photocatalytic performance of the M-phase fibers by placing the sample vial directly in the UV oven. This setup and procedure were similar to that for the D-phase fibers, and it was performed over two continuous cycles. (#1 and #2)
    - Another set of experiments (#3 and #4) was designed to quantify the photocatalytic degradation due to UV illumination through the core only. In this case, only the uncoated fiber core was exposed to UV light, whereas the rest of the sample vials were protected using an aluminum foil.
- A control of MB solution photodegradation upon UV exposure in the absence of fibers was also tested.

CHAPTER 4.

RESULTS AND DISCUSSION

4.1 Structural and Optical Properties

4.1.1 Thermal Properties of PMMA raw material

The characteristic properties of the polymer play a vital role in influencing the fiber morphology. DSC and TGA were performed to characterize the thermal transition of the as-obtained raw material. As seen in **Figure** 9a, PMMA begins to degrade after 300°C. Therefore, the polymer should never encounter any temperature higher than 300°C. It also serves as the limiting temperature for melt spinning (relevant to S_M). The DSC curve indicates (**Figure** 9b) that PMMA raw material is amorphous. Amorphous materials exhibit poor polymer chain entanglement, which results in the formation of fiber without mechanical durability.

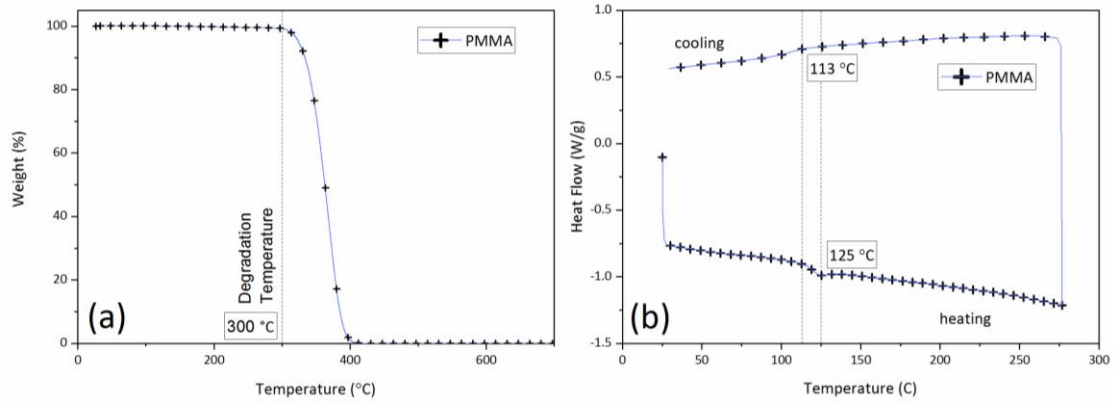

Figure 9. Thermal Properties of PMMA raw material. (a) TGA and, (b) DSC, Glass Transition Temperature was Between 113°C and 125°C

4.1.2 Fabrication of Porous Structure Using Phase Inversion

Porous morphology in photocatalytic support structures improves the contaminant mass transport. Both the D-phase and M-phase fiber comprise a porous matrix. It was fabricated using phase inversion. In this section, the process variables influencing the pore morphology are described. Phase inversion involves a polymer/solvent solution coming in contact with a non-solvent or coagulant. Based on the solvent-coagulant diffusion kinetics, different pore morphologies can be obtained. In this section, the selection of solvent and coagulant is described for the optimization of porous structures.

Selection of Solvent: The fabrication procedure of thin films is described in **Figure** 10a. Films were prepared by pouring the solution over the glass slide using a syringe and then immediately dipped in the coagulant bath. The dipping technique was used due to its similarity associated with coagulation during wet spinning. Films were fabricated instead of fibers so that the microstructure could be easily observed using an optical microscope. Although the detailed aspects of film making differ from fiber spinning, the findings of the analysis will be qualitatively applicable. To identify the appropriate solvent and non-solvent, two solvents (i.e., DMAc and THF) and three coagulants (i.e., water, methanol, and hexane) were examined in this study. The solvent set comprised of a volatile solvent (i.e., THF, boiling point 66°C) and non-volatile solvent (i.e., DMAc, boiling point 165°C). Coagulants with different degrees of miscibility were selected, with water being the most hydrophilic and hexane being the least hydrophilic. Six kinds of single-phase

films were fabricated using every possible combination of solvent and coagulant, as shown in **Figure** 10b.

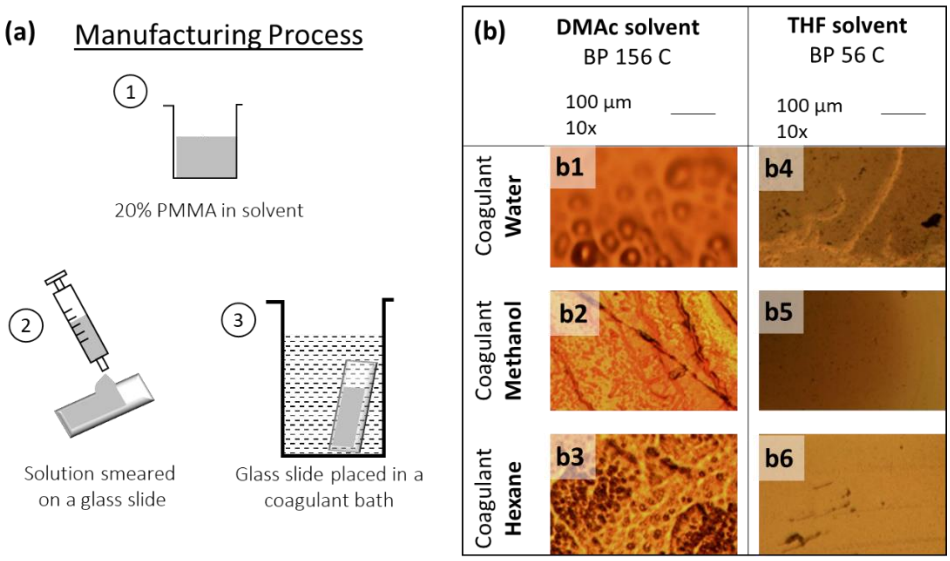

Figure 10. (a) Film fabricated using Phase Inversion Technique. (b) Optical Microscopy Images of Films Prepared using Stated Solvent/Coagulant Combination

The films fabricated using DMAc solvent (**Figure** 10b1-b3) indicate a corrugated or porous structure. Whereas the films fabricated using THF (**Figure** 10b4-b6) indicate a smooth, nonporous surface. The difference in film morphology was attributed to the volatility of the solvent. The mechanism for film formation in **Figure** 10b1-b3 was primarily polymer precipitation by solvent and non-solvent exchange, which inherently forms a porous structure. While the films in **Figure** 10b4-b6 were formed predominantly by solvent evaporation. THF being volatile at room temperature instantaneously increased the polymer concentration at the solvent-coagulant front, which prevented nucleation of voids.[68] It resulted in a dense and surface smooth film devoid of pores.

Therefore, a non-volatile solvent (i.e., DMAc) was selected for creating porous structures using phase inversion.

Selection of Non-Solvent or Coagulant: After identifying DMAc as a suitable solvent, the next step was the selection of an appropriate coagulant. The expectation from the fiber spinning method was to obtain collectible fibers with a well-defined cylindrical structure, to the advantage of a three-dimensional porous structure. For identifying a suitable coagulant, fibers were solution-spun using 25 wt% PMMA/DMAc solution and precipitated in different coagulant bath, as shown in **Figure** 11a. The solution extruded into the water coagulation bath only demonstrated a fiber structure (**Figure** 11 b1), whereas in cases of methanol (**Figure** 11 b2) or hexane (**Figure** 11 b3), the solution sank into the bottom of the beaker forming a lump. The driving forces for retaining the structural integrity during solution spinning is the affinity between the solvent and non-solvent. The best fiber structure is observed with water since it has the highest affinity towards DMAc amongst the coagulants. The structural integrity of the fiber can be seen in **Figure** 11c since the fiber can be picked up by a tweezer. SEM image (**Figure** 11d) of the fiber shows that the fiber is porous. Commercially obtained PMMA is transparent, but the fabricated fibers had a distinct white color. The complex porous structure observed in the SEM was responsible for reflecting light giving it a distinctive white color.

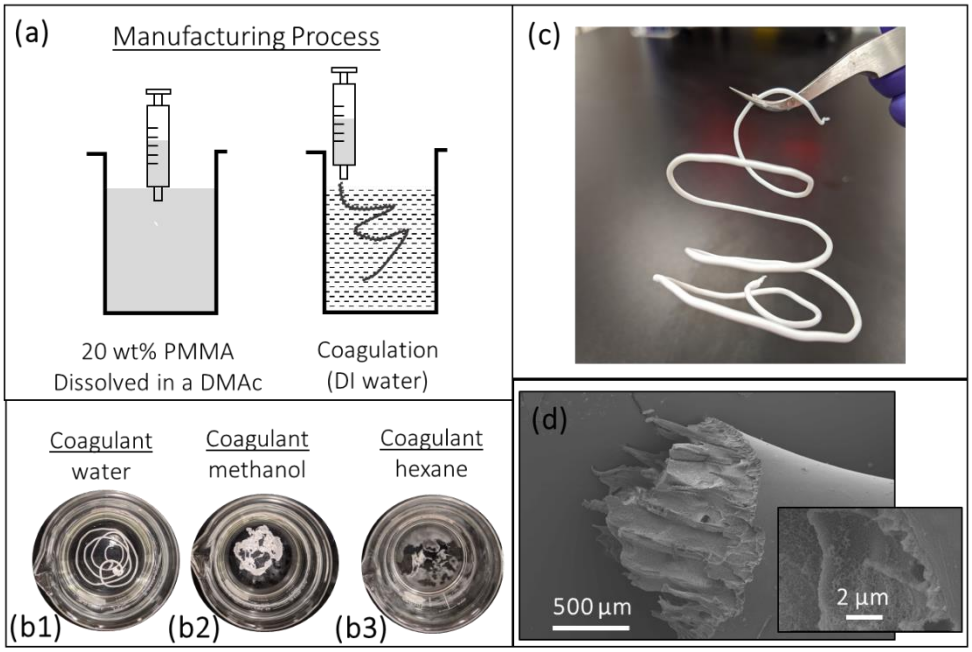

Figure 11. (a) Solution Spinning of S-phase (SS) fibers, (b) Pictures of Fibers After Coagulation in (b1) Water (b2) Methanol, and (b3) Hexane. (c) SS Prepared using Water Show A Fiber-Like Structure (d) SEM of SS Shown in (c)

4.1.3 Optical Properties of the Porous Matrix

For improvement in photocatalytic performance, both high surface area and light accessibility are desired. In the previous section, the fabrication of porous fibers was described, which entailed a high surface area. However, pores are imperfections capable of scattering light[73], and it can interfere with the light transport needed for photocatalysis. In this section, the optical properties of the porous matrix fiber are characterized.

Bandgap of Titania: The bandgap is purchased titania nanoparticle was measured using UV-vis, as shown in **Figure** 12. The absorbance spectrum is indicated in **Figure** 12a. Commercially obtained titania is an indirect bandgap semiconductor.[74,75] Therefore the

absorbance spectrum is converted to a Tauc plot (**Figure** 12b) using the following relation-

$$\alpha(E) \propto \left(E - E_g\right)^2$$

Absorption for photons with energy higher than 3eV (i.e., intercept indicated in the Tauc plot (**Figure** 12b). Therefore, the bandgap of the semiconductor is approximately 3eV (413 nm). This falls in the ultraviolet range. An ideal substrate for anchoring titania must be transparent to radiation of wavelength less than or equal to 413 nm.

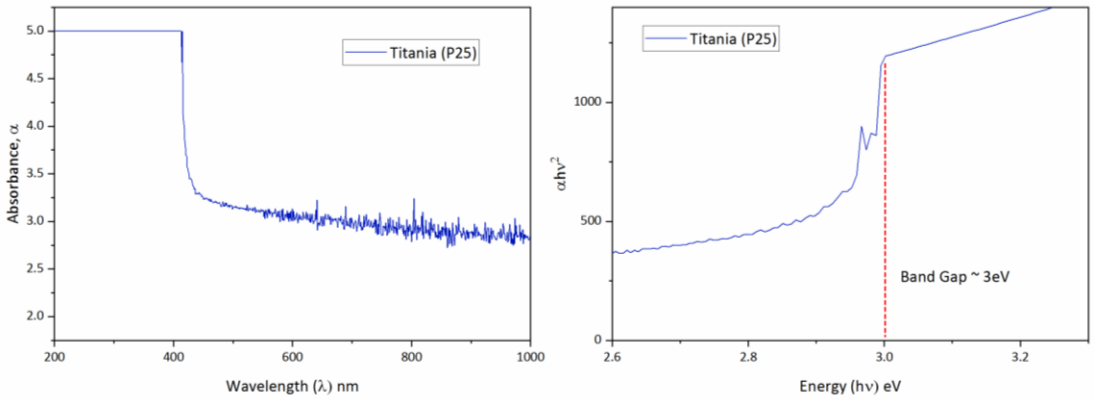

Figure 12. Optical Properties of Titania (P25) Raw Material (a) Absorbance Spectrum (b) Tauc plot for Calculating Bandgap

Optical Properties of Porous Substrate: Both the D-phase and M-phase comprise a porous matrix. The entire D-phase fiber was entirely porous, whereas the M-phase fiber had a porous shell. The porous matrix in each of the cases was created using phase inversion. In this section, the optical properties of pores created using phase inversion are described. Three film samples were analyzed to understand the influence of pores on optical properties systematically. The first was a solid PMMA film (PMMA-1) prepared by casting. The second is a porous PMMA film (PMMA-2) prepared by phase inversion

similar to the film studied in section 4.1.2. The third is a porous PMMA film with anchored titania (PMMA-3) prepared by phase inversion. Titania is anchored in the substrate by adding 12.5 wt% titania to the 25 wt% PMMA/DMAc solution (i.e., 12.5 g titania, 25 g PMMA and 100 ml DMAc) and then coagulating the dispersion. The optical properties of the three films were characterized using UV-vis, as shown in **Figure** 13. The absorbance and transmittance graphs are directly obtained from the UV-vis instrument. The reflectance curve is plotted using the following equation-

$$R = 1 - A - T$$

Here, *R, A, T* are the fraction of radiation reflected, absorbed ($= \frac{\alpha}{\alpha_{max}}$) and transmitted, respectively. PMMA-1 was observed to be transparent to radiation of wavelength 250 nm and above. Since PMMA-1 shows no obvious indication of pores, the optical properties are intrinsic to the material. Since no inter or intra-band electronic transitions are observed in the UV range, PMMA is suitable for anchoring titania. PMMA-2 had less than 1% transmittance (**Figure** 13b), which shows the impact of pores on the substrate. The reflectance of PMMA-2 was ~50% for radiation of wavelength 250 nm or above (**Figure** 13c). Therefore, PMMA-2 shows reduced transmittance through the thickness of the film but scatters ~50% of the radiation falling on its surface (**Figure** 13c). If titania is anchored on the porous surface, then the scattered radiation is available for titania to absorb. The optical properties of PMMA-3 indicate a similar property. The reflectance curve of PMMA-3 is shifted concerning the reflectance curve of PMMA-2. This means that the anchored titania indeed absorbs radiation scattered by the porous surface. From these results, it was concluded that the porous structure was suitable for anchoring titania.

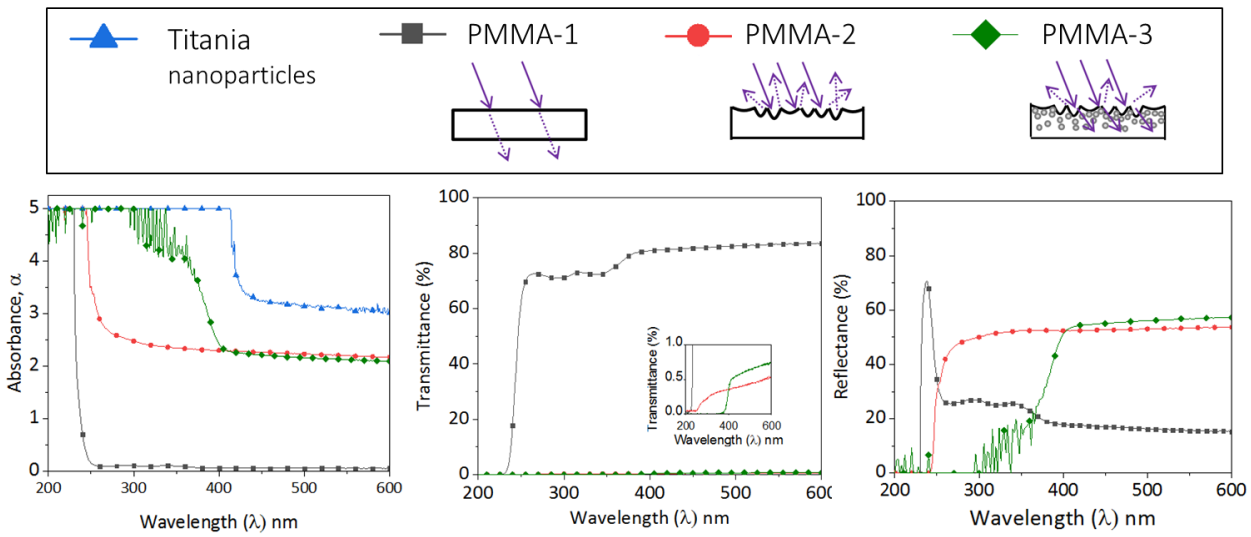

Figure 13. Optical Properties of PMMA-Based Films

4.2 D-phase fibers

4.2.1 Structural-Property relationship

In section 4.1.2, DMAc and water were identified as suitable choices for solvent and non-solvent, respectively. In this section, the overall structural properties of the D-phase fibers (D_5 and D_{10}) are described. Two samples of D-phase fibers with different fiber diameters were studied to understand the influence of fiber sizes on morphology (porosity and titania dispersion) and following photocatalysis effects.

The fiber samples were prepared by extruding the composite solution spinning dope using different nozzle diameters (i.e., 0.5 mm and 1.0 mm). There is uncertainty associated with the titania concentration post coagulation since it can be washed away during the solvent/non-solvent interaction. The TGA results (**Error! Reference source not found.**a) indicate that titania is indeed preserved in the fibers and has an average wt% of ~36, which was slightly higher than the wt % in the solution spinning dope (,PMMA:

TiO_2 weight ratio of 2:1) and can be attributed to dispersion quality along the fibers. The SEM images of the fiber cross-section indicate a complex porous structure (**Figure** 14i). At zoom-in image (**Figure** 14ii) shows titania clusters were dispersed in the porous PMMA matrix. The fiber constituents are indicated in the EDS spectrum (**Figure** 14iii), gold (Au) was representative of the 15 nm conductive gold coating from SEM sample preparation. Overall, titania was uniformly dispersed across the cross-section, as observed in the EDS TiK map (**Figure** 14v).

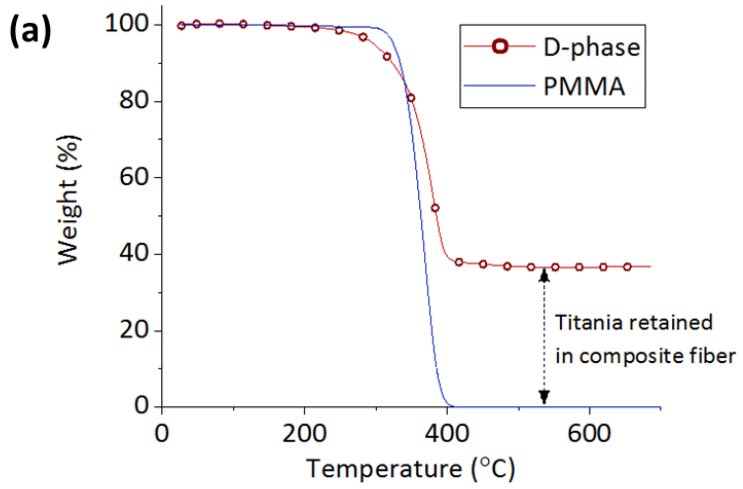

(b)

Sample Name	Titania wt % in solvent	BET specific surface area	Titania wt % after coagulation
D-phase D_5	33.3%	33.2 m^2/g	36.8%
D-phase D_{10}	33.3%	17.4 m^2/g	36.4%

Figure 14. (a) TGA to Quantify Titania Retention in D-phase (b) BET results for the D-phase Fibers

The porous morphology of the fibers was sensitive to nozzle diameter. D_5 had approximately two times higher BET specific surface area compared to D_{10} that has a similar diameter and surface area to the S_s fibers (**Error! Reference source not found.**c).

Coagulation dynamics were observed to be sensitive to fiber size. As the coagulant encounters the solution, a precipitated skin layer was formed, which serves as a hindrance for further solution-coagulant interaction. In this process, radial channels are formed from leaching out the solvent, as shown in **Figure** 14a and 15b (i and ii). These radial channels were responsible for the porous structure. The channels bisect and get narrower as the coagulant penetrates deeper into the fiber, as described in the schematic (**Figure** 14a and 15b, iii). In the case of the smaller diameter fiber (D_5), the coagulant needs to penetrate a shorter radial distance. This causes the leaching process to experiences a lower resistance as it penetrates deeper into the cross-section. Therefore, higher porosity was observed for smaller fiber diameter.

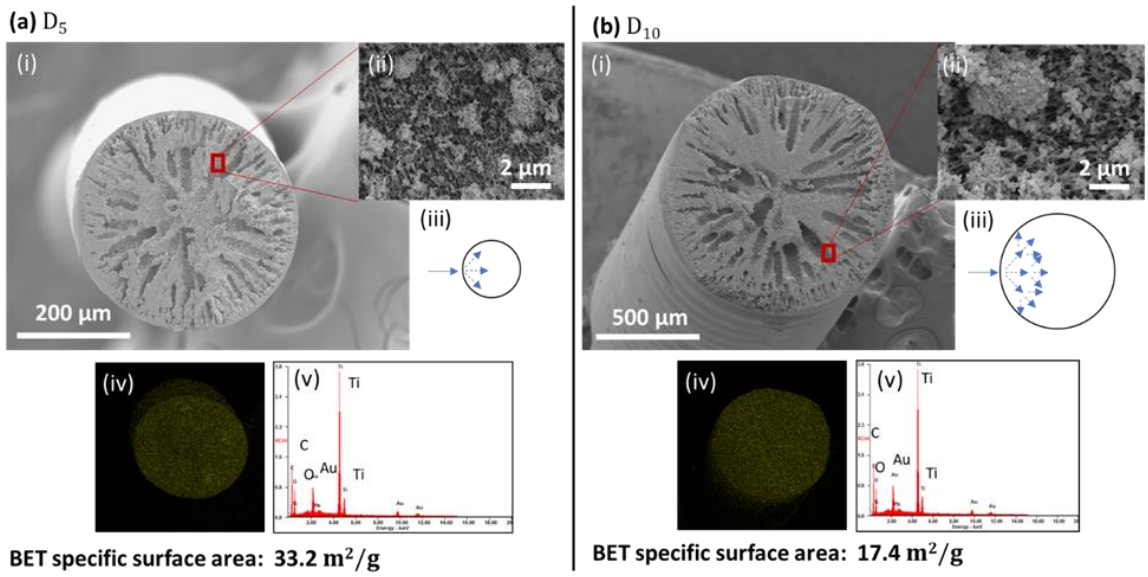

Figure 14. Structural Properties of D-phase Fibers (i) SEM of Cut Cross-Section (ii) Zoom-In of Porous Structure (iii) Schematic Sketch of Coagulant Encroachment Within the Fiber Cross-Section (iv) EDS TiK Elemental Map and (v) EDS Spectrum. The Above Tests were Conducted for Two Fiber Samples (a) D_5 and (b) D_{10}

4.2.2 Photocatalytic Performance

The photocatalytic performance of D-phase fibers (D_5 and D_{10}) was measured using the procedure described in Section 3.4. A picture of the fiber samples is shown in **Figure** 15.

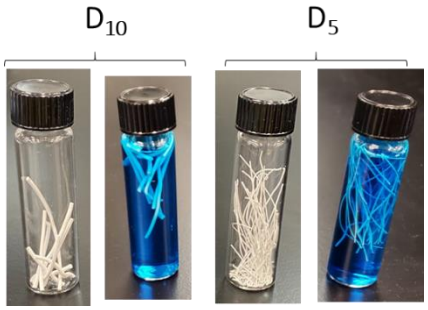

Figure 15. D-phase Samples

The dye concentration during UV exposure was monitored and showed in **Figure** 16a. In the first experiment (#1), freshly fabricated fibers were used until the MB solution became colorless. In the second experiment (#2), the fiber used in the first experiment were dried in the oven at 60°C for 24 hours, and then the experiment was repeated. The intent of experiment #2 is to quantify the reusability of the fibers.

The parametric fitting curves considering the first-order kinetics model are listed in **Figure** 16. MB degradation requires adsorption on the catalyst surface and followed by photocatalytic degradation. During the 5-day soaking period, the MB concentration in the solution reduced since the porous matrix adsorbed a portion of the dye. This dye concentration before UV exposure is represented by 'C_o' and was equal to the y-axis intercept in **Figure** 16a. D_5 being more porous (indicated by BET) compared to D_{10}, demonstrates better photocatalytic performance. D_5 shows a lower C_0 (0.7 mg/L) and

higher k (0.116 min^{-1}) as compared to D_{10}. In #2, the degradation kinetics is slower compared to #1. This indicates fouling in the fibers. Reduction in C_0 means fewer catalyst sites are available, indicating that the adsorbed dye from #1 experiment was not completely decomposed by titania. Fewer catalyst sites translated to lower degradation rate k. The decrease in the degradation rate was higher for D_5, indicating more fouling. In this study, porosity was identified as a key characteristic that influenced the photocatalytic performance. Higher porosity improved photocatalytic performance but showed poor UV accessibility, which resulted in higher pore fouling.

Langmuir-Hinshelwood
Pseudo First Order Kinetics Model

$$\ln\left(\frac{C}{C_o}\right) = -kt$$

Expt	Sample	k (min^{-1})	Co (mg/L)
Control	MB	0.0043	3.200
#1	D_{10}	0.053	2.466
#2		0.023	3.141
#1	D_5	0.116	0.706
#2		0.044	3.000

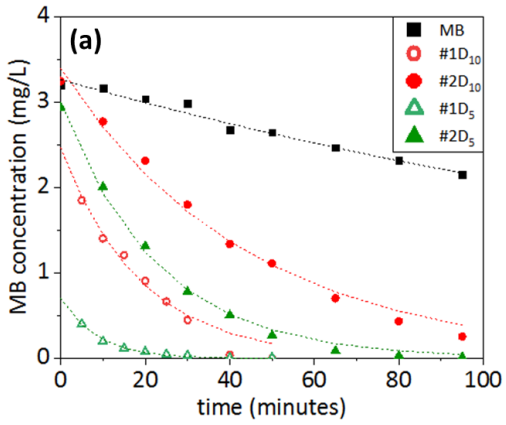

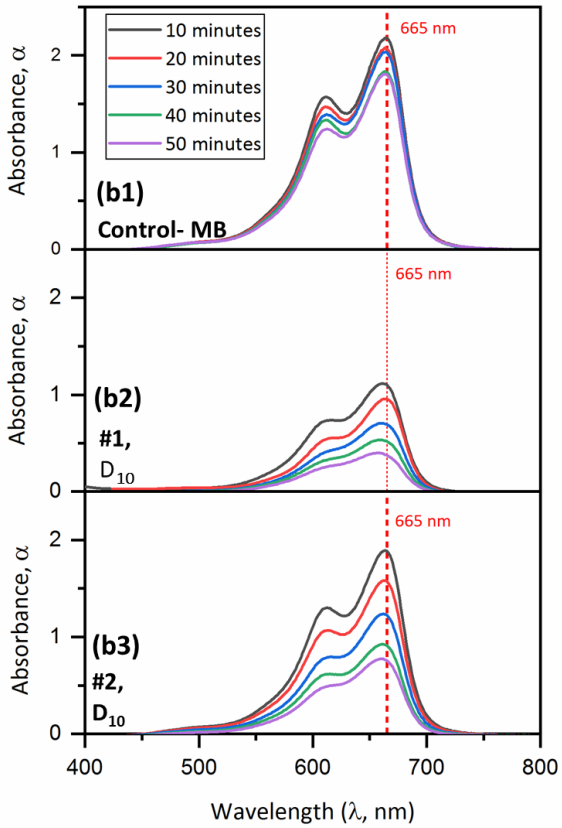

Figure 16. Photocatalytic Reaction Kinetics was Analyzed using a Pseudo-First-Order Kinetics Model. Parameters C_0 and k were Obtained Using Regression Fit, (a) Graph Representing Degradation as a Function of Time (b) UV-vis Absorbance

Spectrum for MB Degradation (b1) Only MB Solution, (b2) D_{10} , expt. #1 and (b3) D_{10}, expt #2

4.3 M-phase Fibers

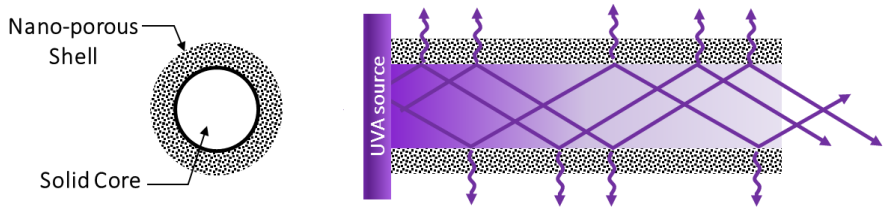

Figure 17. Schematic Sketch of M-phase Fibers (CS_M)

The M-phase fibers had a core-shell architecture (i.e., CS_M) comprising of a solid PMMA core and a porous PMMA-titania composite shell. The core serves as a radially emitting optical fiber that provides remote UV accessibility, and the porous shell anchors the catalyst (titania). A sketch illustrating the core's utility is shown in **Figure** 17. Compared to D-phase, the M-phase has an additional route for light transport.

4.3.1 Structure-Property Relationship

The different phases of CS_M have different functionalities. The fiber core via the melt extrusion method (i.e., S_M) is UV transparent to propagate light remotely. S_M also serves as a structural component for supporting the porous coating due to its mechanical durability as compared to the solution-spun fibers. The fiber shell is similar in composition and functionality as the D-phase fibers (**Figure** 18). The fiber porosity is sensitive to the fabrication procedure; therefore, the porosity is characterized using BET.

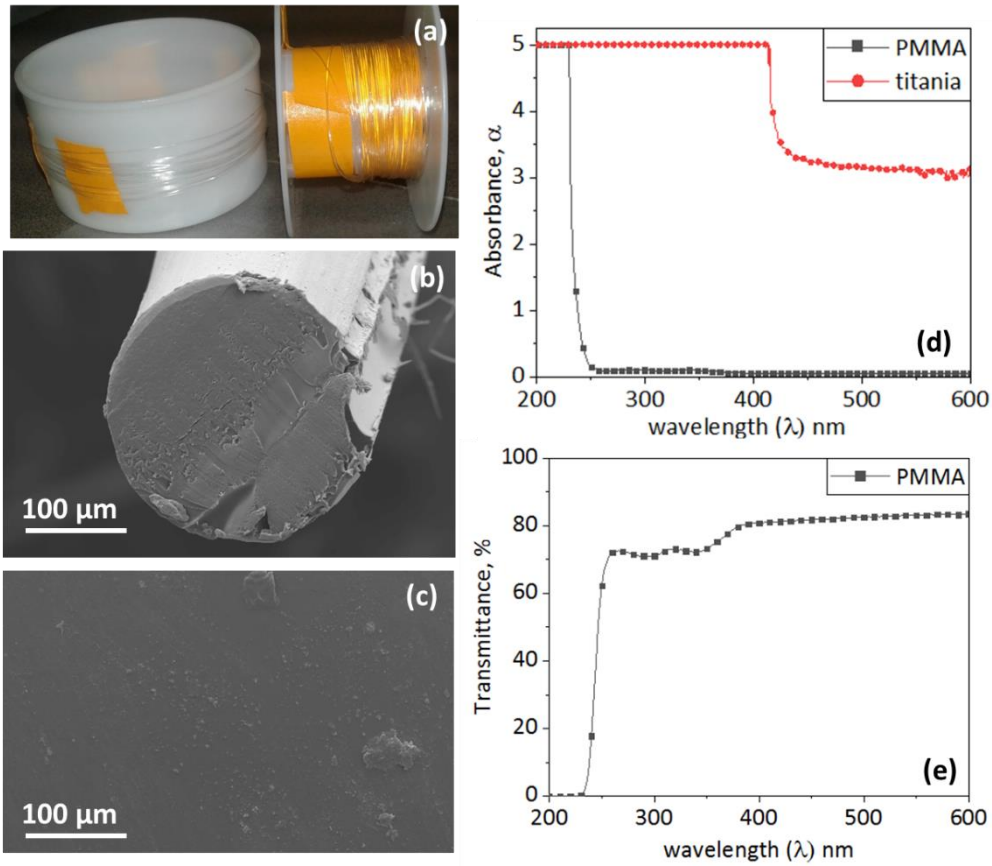

Figure 18. (a) Picture of CS_M Core or S_M Fiber (b) SEM of S_M (c) SEM of the Film Prepared By Casting (d) UV-vis Absorbance Spectrum and, (e) UV-vis Transmittance Spectrum

Fiber Core (S_M): S_M is fabricated using a melt spinning technique using a screw extruder. The extruded fiber was drawn using an automatic winder. Only one fiber diameter was obtained with the maximum drawing and fiber stability during the winding and extrusion procedures. The overall fiber diameter ranged as 0.24 mm ± 0.02 mm. This was estimated by measuring the fiber diameter at 25 locations using a vernier caliper across a span of 2.7 cm span. S_M fiber was transparent (**Figure** 18a), similar to commercially obtained PMMA. A close-up view of the fiber (SEM, **Figure** 18b) shows a densely packed structure devoid of pores. The optical properties of the fiber were

characterized using UV-vis. Due to limitations related to fiber size, PMMA films were cast and analyzed in UV-vis. Even though the cast PMMA films are fundamentally different from melt-spun fibers, the qualitative observations of the PMMA films should apply to PMMA fibers (S_M). To reassure the validity of this technique, SEM is performed for the cast film (**Figure** 18c) as well. Both the SEMs (**Figure** 18 b-c) show that the melt-spun fiber and cast film show similar dense structures. The UV-vis absorbance spectrum (**Figure** 18d) does not intersect with the absorbance of titania (P25). It means no inter or intra-band transitions of PMMA are expected to occur while interacting with light with a wavelength greater than or equal to 250 nm. The transmittance spectrum (**Figure** 18e) shows that PMMA ~80% transparent to light of wavelength greater than or equal to 250 nm. Ultimately, the fiber should be able to transport UV radiation of a wavelength of 365 nm since it is dominant wavelength from the UV source (UV oven). Therefore, the fiber core (S_M) was suitable for light transport.

Fiber Shell: The CS_M shell is compositionally similar to D-phase. The porous structure was prepared by phase inversion during dip coating. The SEM image (**Figure** 19a) shows that the shell was a highly porous matrix with dispersed titania nanoparticles. The EDS map (**Figure** 19b) shows that titania was uniformly dispersed across the shell cross-section. The BET tests (inset in **Figure** 19b) indicate a specific surface area of 15.7 m^2/g. It is slightly lower than the BET SSA of the D-phase. The reduction in specific surface area is because of different solvent-coagulant interaction dynamics during dip coating compared to solution spinning. Inferring from the BET results, the number of active sites

for adsorption was lowest for M-phase (**Figure** 19), comparing with D-phase (Section 4.1.2, **Figure** 14). However, the architecture of the M-phase entails better light accessibility compared to D-phase since UV light can impinge on the porous structure both internally (through fiber core, S_M) and externally (similar to D-phase).

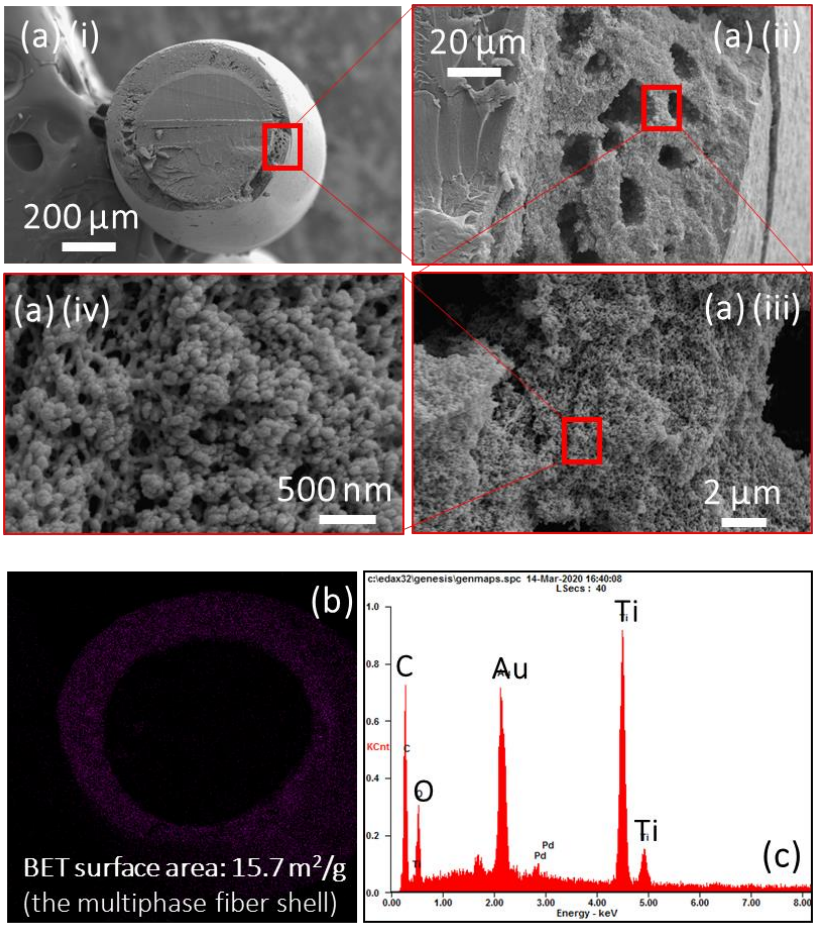

Figure 19. Structural Properties of CSM (a) SEM (b) EDS Map of TiK (c) EDS Spectrum

Mechanical Properties: The mechanical property of the fiber was characterized using a tensile test. PMMA, as an amorphous polymer, was unsuitable for load carrying applications. The intent of the tensile test was to show that PMMA fiber was not fragile.

The box plot (**Figure** 20a) shows that the uncoated fibers (S_M) and coated fibers (CS_M) had an average elastic modulus of ~3.26 GPa and ~7.52 GPa, respectively. S_M shows a lower variance compared to CS_M, which is attributed to the non-uniformity associated with the manual dip-coating process. The stress-strain characteristics are shown in **Figure** 20b, which indicates that the fibers stretch and display necking before failure. This concludes that CS_M is ductile and sturdy.

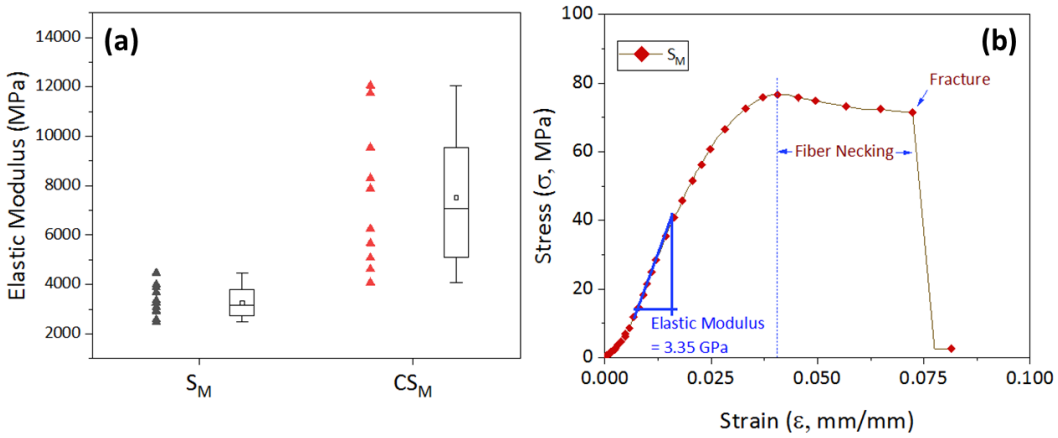

Figure 20. Mechanical Properties (a) Elastic Modulus for Uncoated Fiber (S_M) and Coated Fiber (CS_M) (b) Stress-Strain Relation of S_M

4.3.2 Photocatalytic Performance

The photocatalytic performance of CS_M was measured using the procedure described in Section 3.4. A picture of the fiber sample is shown in **Figure** 21b. The fibers were kept in an 8ml glass vial and the uncoated fiber length hangs from the open end of the vial. The extra length of the uncoated fiber was provided to support the fiber inside the glass vial. Two experiments were conducted for analyzing the photocatalytic performance- overall performance and effectiveness of the fiber core.

Overall Photocatalytic Performance: This experiment set was similar to the experiment performed on the D-phase (section 4.2.2). The change in MB concentration during UV exposure is plotted in **Figure** 21c. Two experimental trials (#1 and #2) were conducted. In the first experimental trial (#1), the freshly prepared CS_M fibers were used. The sample was exposed to UV until MB solution became colorless. In the second experimental trial (#2) , the fibers from #1 were dried in the oven for 80°C for 24 hours and reused. From #1, the parameters 'C_0' and 'k' for CS_M were comparable to D_{10}. Since porosity of CS_M and D_{10} are comparable, the same is translated to the degradation results. The 'k' (i.e., 0.059 min^{-1}) in CS_M was slightly higher than that in D_{10} (i.e., 0.053 min^{-1}), in spite of D_{10} possessing with slightly higher porosity. This was due to the superior architecture of the M-phase that provided better UV-accessibility. From #2 results, the performance was observed to depreciate, indicating fouling. 'k' of CS_M reduced from 0.059 min^{-1} to 0.036 min^{-1} (i.e., 39%) from cycle 1 to cycle 2. But, the depreciation was not as severe as D_{10} (i.e., 57%, from 0.053 min^{-1} to 0.023 min^{-1}) and D_5 (i.e., 62%, from 0.116 min^{-1} to 0.044 min^{-1}). Therefore, CS_M was more resistant to fouling than the other samples.

Effectiveness of Fiber Core: The uniqueness of the M-phase was the presence of the optical fiber core (S_M). This experiment was designed to quantitatively estimate the contribution of remote light transport through this architecture. A fresh sample of CS_M was prepared for this experiment, containing ~50 mg of titania like the earlier samples. The sample vial was covered with an aluminum foil, as shown in **Figure** 21b #3 and #4. Only the uncoated fiber tip was exposed, so that catalyst activation was limited to light

transmission from the fiber core. The degradation rate 'k' from #3 is 0.0077 min^{-1} which is ~13% of the overall photocatalytic degradation rate (dividing k from #3 with k from #1). The degradation was observed to saturate in 60 minutes. Then the sample was placed in the dark for another 24 hours then exposed to UV light. This change in MB concentration during the second cycle of UV exposure is plotted as #4. Resting the sample in the dark caused the MB concentration to reduce from 0.812 mg/L to 0.584 mg/L. Therefore, contaminant degradation by UV exposure purged the adsorbed sites and made it available for reuse. This experiment concluded that the presence of fiber core improved the overall photocatalytic performance.

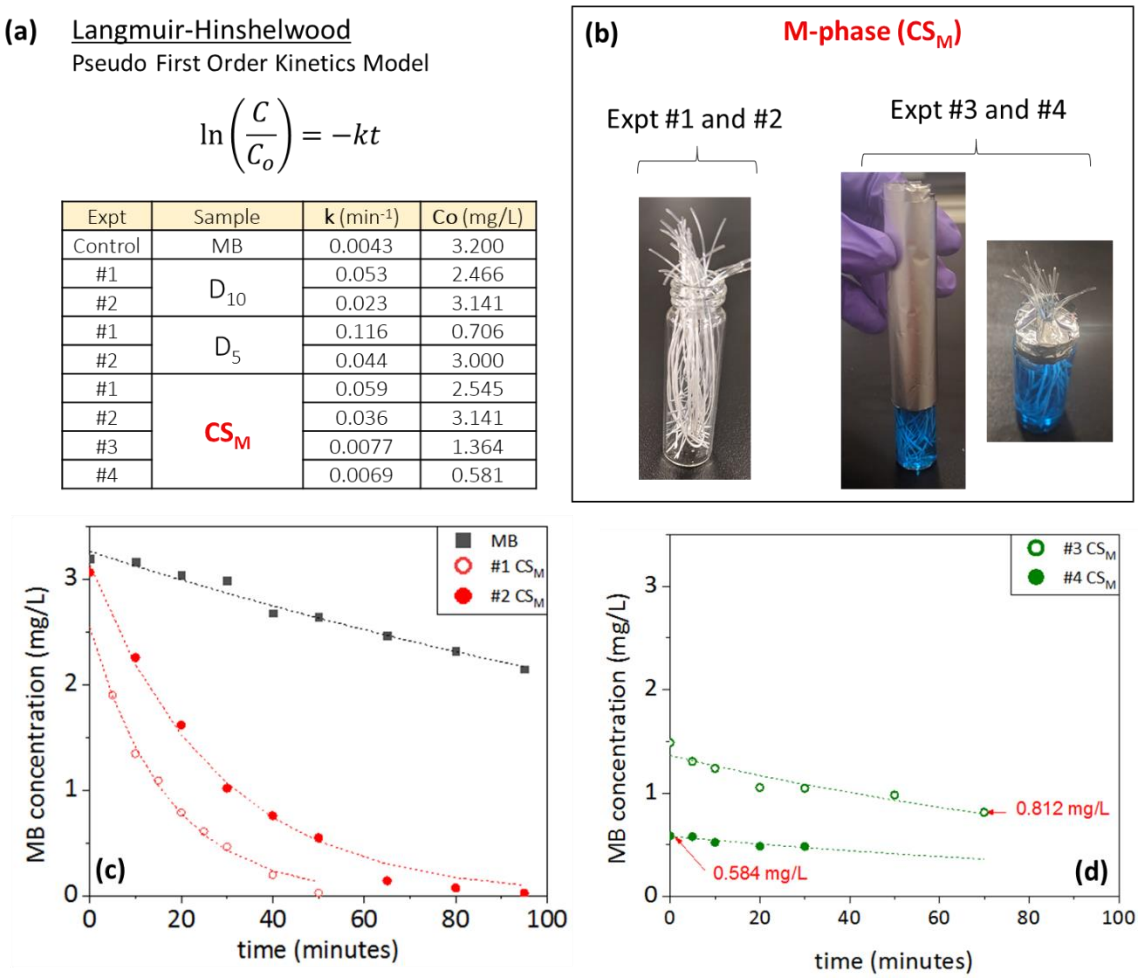

Figure 21. Photocatalytic Degradation Kinetics of CS_M (a) Parameters Obtained from Regression Fit (b) Samples used for Experiments, (c) and (d) Photodegradation Curves

4.4 Photocatalytic Performance Summary

In the previous sections (4.2.2 and 4.3.2), the photocatalytic performance of D-phase and M-phase fiber samples were individually described. Here, all the observations are summarized, and insights about the catalysis process are drawn. Overall, three samples were studied D_5, D_{10}, and CS_M. Their catalytic performance was analyzed using Langmuir-Hinshelwood pseudo-first-order degradation kinetics. The parameters are

plotted as a function of BET SSA, as shown in **Figure** 22. BET SSA shows a negative correlation with C_0 and a positive correlation with k. For better photocatalysis, C_0 should be low and k should be high, indicating high porosity is desirable. In this study, the best photocatalytic performance was demonstrated by D_5 since it is the most porous. Porosity improves adsorption by providing more sites for the catalytic reaction. CS_M demonstrated a better degradation rate than D_{10} despite having a relatively lower porosity. This was due to M-phase architecture, which provided better UV accessibility. Fibers must also be reusable for commercial adaptation. Reusability can be described as the gap between the two curves (#1 and #2). The smallest gap was observed for $CS_{M,}$ indicating the best reusability amongst the samples. Reusability was also qualitatively similar to the UV accessibility since UV light was responsible for decomposing the adsorbed contaminants making the sites available for reuse.

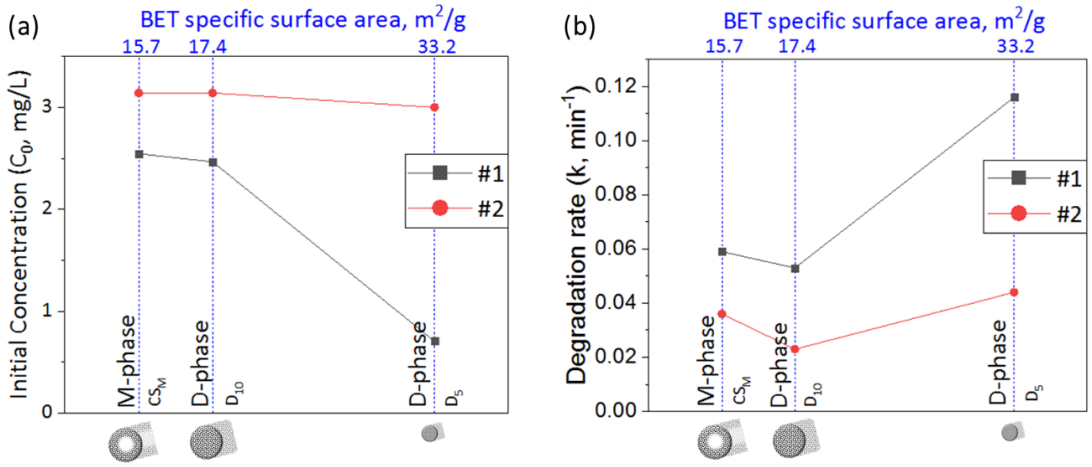

Figure 22 Photocatalytic Degradation Parameters (a) C_0, and (b) k Analysed as a Function of BET SSA

CHAPTER 5.

CONCLUSION

Fibers were successfully fabricated as photocatalytic support structures using a low-cost and scalable manufacturing technique. The photocatalytic performance of the fibers was also quantified. Manufacturing of photocatalytic support structures was observed to be an optimization problem. The presence of pores improved mass transport but reduced UV accessibility. Among the tested samples, D_5 reported the best photocatalytic performance (i.e., k= 0.116 min^{-1}) due to its high porosity that enabled better mass transport. CS_M (i.e., k= 0.059 min^{-1}) demonstrated better degradation rate compared to D_{10} (i.e., k= 0.053 min^{-1}), in spite of having a higher BET SSA for the latter. This was due to the superior architecture of M-phase that enabled better light transport. For the development of a viable support structure, three parameters must be optimized- increase adsorption, improve UV accessibility and reusability of product. In this work, adsorption was enhanced through porosity, and UV accessibility was enhanced using core-shell fiber architecture. Reusability was qualitatively similar to UV accessibility since UV light was responsible for degrading the adsorbed contaminants making the sites available for reuse. Future work should focus on optimizing the fiber size, pore morphology, and porosity control to improve the photocatalytic performance further.

REFERENCES

(1) Singh, S.; Ramakrishna, S.; Singh, R. Material Issues in Additive Manufacturing: A Review. *J. Manuf. Process.* **2017**, *25*, 185–200. https://doi.org/10.1016/j.jmapro.2016.11.006.

(2) Jin, Y.; M Granville, A. Polymer Fiber Optic Sensors – A Mini Review of Their Synthesis and Applications. *J. Biosens. Bioelectron.* **2016**, *07* (01), 1–11. https://doi.org/10.4172/2155-6210.1000194.

(3) Shannon, M. A.; Bohn, P. W.; Elimelech, M.; Georgiadis, J. G.; Marĩas, B. J.; Mayes, A. M. Science and Technology for Water Purification in the Coming Decades. *Nature* **2008**, *452* (7185), 301–310. https://doi.org/10.1038/nature06599.

(4) Lee, C. G.; Javed, H.; Zhang, D.; Kim, J. H.; Westerhoff, P.; Li, Q.; Alvarez, P. J. J. Porous Electrospun Fibers Embedding TiO 2 for Adsorption and Photocatalytic Degradation of Water Pollutants. *Environ. Sci. Technol.* **2018**, *52* (7), 4285–4293. https://doi.org/10.1021/acs.est.7b06508.

(5) Malik, H. H.; Darwood, A. R. J.; Shaunak, S.; Kulatilake, P.; El-Hilly, A. A.; Mulki, O.; Baskaradas, A. Three-Dimensional Printing in Surgery: A Review of Current Surgical Applications. *J. Surg. Res.* **2015**, *199* (2), 512–522. https://doi.org/10.1016/j.jss.2015.06.051.

(6) Parandoush, P.; Lin, D. A Review on Additive Manufacturing of Polymer-Fiber Composites. *Compos. Struct.* **2017**, *182*, 36–53. https://doi.org/10.1016/j.compstruct.2017.08.088.

(7) Xu, W.; Jambhulkar, S.; Verma, R.; Franklin, R.; Ravichandran, D.; Song, K. In Situ Alignment of Graphene Nanoplatelets in Poly(Vinyl Alcohol) Nanocomposite Fibers with Controlled Stepwise Interfacial Exfoliation. *Nanoscale Adv.* **2019**, *1* (7), 2510–2517. https://doi.org/10.1039/c9na00191c.

(8) Tekinalp, H. L.; Kunc, V.; Velez-Garcia, G. M.; Duty, C. E.; Love, L. J.; Naskar, A. K.; Blue, C. A.; Ozcan, S. Highly Oriented Carbon Fiber-Polymer Composites via Additive Manufacturing. *Compos. Sci. Technol.* **2014**, *105*, 144–150. https://doi.org/10.1016/j.compscitech.2014.10.009.

(9) Ng, L. Y.; Mohammad, A. W.; Leo, C. P.; Hilal, N. Polymeric Membranes Incorporated with Metal/Metal Oxide Nanoparticles: A Comprehensive Review. *Desalination* **2013**, *308*, 15–33. https://doi.org/10.1016/j.desal.2010.11.033.

(10) Song, K. *Micro- and Nano-Fillers Used in the Rubber Industry*; Elsevier Ltd, 2017. https://doi.org/10.1016/B978-0-08-100409-8.00002-4.

(11) Fujishima, A.; Rao, T. N.; Tryk, D. A. Titanium Dioxide Photocatalysis. *J. Photochem. Photobiol. A Chem.* **2000**, *1* (21). https://doi.org/10.1016/S1389-5567(00)00002-2.

(12) Zhang, Y.; Jiang, Z.; Huang, J.; Lim, L. Y.; Li, W.; Deng, J.; Gong, D.; Tang, Y.; Lai, Y.; Chen, Z. Titanate and Titania Nanostructured Materials for Environmental and Energy Applications: A Review. *RSC Adv.* **2015**, *5* (97), 79479–79510. https://doi.org/10.1039/c5ra11298b.

(13) Nonami, T.; Hase, H.; Funakoshi, K. Apatite-Coated Titanium Dioxide Photocatalyst for Air Purification. *Catal. Today* **2004**, *96* (3), 113–118. https://doi.org/10.1016/j.cattod.2004.06.112.

(14) Tu, W.; Zhou, Y.; Liu, Q.; Tian, Z.; Gao, J.; Chen, X.; Zhang, H.; Liu, J.; Zou, Z. Robust Hollow Spheres Consisting of Alternating Titania Nanosheets and Graphene Nanosheets with High Photocatalytic Activity for CO 2 Conversion into Renewable Fuels. *Adv. Funct. Mater.* **2012**, *22* (6), 1215–1221. https://doi.org/10.1002/adfm.201102566.

(15) Wong, C. L.; Tan, Y. N.; Mohamed, A. R. A Review on the Formation of Titania Nanotube Photocatalysts by Hydrothermal Treatment. *J. Environ. Manage.* **2011**, *92* (7), 1669–1680. https://doi.org/10.1016/j.jenvman.2011.03.006.

(16) Chong, M. N.; Jin, B.; Chow, C. W. K.; Saint, C. Recent Developments in Photocatalytic Water Treatment Technology: A Review. *Water Res.* **2010**, *44* (10), 2997–3027. https://doi.org/10.1016/j.watres.2010.02.039.

(17) Singh, S.; Mahalingam, H.; Singh, P. K. Polymer-Supported Titanium Dioxide Photocatalysts for Environmental Remediation: A Review. *Appl. Catal. A Gen.* **2013**, *462–463*, 178–195. https://doi.org/10.1016/j.apcata.2013.04.039.

(18) Shan, A. Y.; Ghazi, T. I. M.; Rashid, S. A. Immobilisation of Titanium Dioxide onto Supporting Materials in Heterogeneous Photocatalysis: A Review. *Appl. Catal. A Gen.* **2010**, *389* (1–2), 1–8. https://doi.org/10.1016/j.apcata.2010.08.053.

(19) Yang, L.; Zhou, S.; Wu, L. Preparation of Waterborne Self-Cleaning Nanocomposite Coatings Based on TiO2/PMMA Latex. *Prog. Org. Coatings* **2015**, *85*, 208–215. https://doi.org/10.1016/j.porgcoat.2015.04.012.

(20) Peill, N. J.; Hoffmann, M. R. Development and Optimization of a TiO2-Coated Fiber-Optic Cable Reactor: Photocatalytic Degradation of 4-Chlorophenol. *Environ. Sci. Technol.* **1995**, *29* (12), 2974–2981. https://doi.org/10.1021/es00012a013.

(21) Neal, H. O.; Garcia-segura, S.; Hristovski, K.; Westerhoff, P. Compact Light-Emitting Diode Optical Fiber Immobilized TiO2reactor for Photocatalytic Water Treatment. *Sci. Total Environ.* **2018**, *613–614*, 1331–1338. https://doi.org/10.1016/j.scitotenv.2017.09.242.

(22) Raja, V.; Sarma, A. K.; Rao, V. V. R. N. Optical Properties of Pure and Doped PMMA-CO-P4VPNO Polymer Films. *Mater. Lett.* **2003**, *57* (30), 4678–4683. https://doi.org/10.1016/S0167-577X(03)00384-7.

(23) R.M., C.; R., P.; F, G.-M.; Benigno, S. Evaluation of Several Commercial Polymers as Support for TiO2 in Photocatalytic Applications. *Glob. NEST J.* **2014**, *16* (3), 525–535.

(24) Fung-Ching, L.; Da-Ming, W.; Cheng-Lee, L.; Juin-Yih, L. Effect of Surfactants on the Structure of PMMA Membranes. *J. Memb. Sci.* **1997**, *123* (2), 281–291. https://doi.org/10.1016/S0376-7388(96)00243-8.

(25) Wang, D. M.; Lin, F. C.; Wu, T. T.; Lai, J. Y. Formation Mechanism of the Macrovoids Induced by Surfactant Additives. *J. Memb. Sci.* **1998**, *142* (2), 191–204. https://doi.org/10.1016/S0376-7388(97)00322-0.

(26) Naeimirad, M.; Zadhoush, A.; Kotek, R.; Esmaeely Neisiany, R.; Nouri Khorasani, S.; Ramakrishna, S. Recent Advances in Core/Shell Bicomponent Fibers and Nanofibers: A Review. *J. Appl. Polym. Sci.* **2018**, *135* (21), 28–30. https://doi.org/10.1002/app.46265.

(27) Kim, J. J.; Hwang, J. R.; Kim, U. Y.; Kim, S. S. Operation Parameters of Melt Spinning of Polypropylene Hollow Fiber Membranes. *J. Memb. Sci.* **1995**, *108* (1–2), 25–36. https://doi.org/10.1016/0376-7388(95)00148-7.

(28) Kim, J. J.; Jang, T. S.; Kwon, Y. D.; Kim, U. Y.; Kim, S. S. Structural Study of Microporous Polypropylene Hollow Fiber Membranes Made by the Melt-Spinning and Cold-Stretching Method. *J. Memb. Sci.* **1994**, *93* (3), 209–215. https://doi.org/10.1016/0376-7388(94)00070-0.

(29) Puppi, D.; Chiellini, F. Wet-Spinning of Biomedical Polymers: From Single-Fibre Production to Additive Manufacturing of Three-Dimensional Scaffolds. *Polym. Int.* **2017**, *66* (12), 1690–1696. https://doi.org/10.1002/pi.5332.

(30) Daristotle, J. L.; Behrens, A. M.; Sandler, A. D.; Kofinas, P. A Review of the Fundamental Principles and Applications of Solution Blow Spinning. *ACS Appl. Mater. Interfaces* **2016**, *8* (51), 34951–34963. https://doi.org/10.1021/acsami.6b12994.

(31) P. J. Barham; Keller, A. High-Strength Polyethylene Fibres from Solution and Gel Spinning. *J. Mater. Sci.* **1985**, *20*, 2281–2302.

(32) Matabola, K. P.; De Vries, A. R.; Moolman, F. S.; Luyt, A. S. Single Polymer Composites: A Review. *J. Mater. Sci.* **2009**, *44* (23), 6213–6222. https://doi.org/10.1007/s10853-009-3792-1.

(33) Teo, W. E.; Ramakrishna, S. A Review on Electrospinning Design and Nanofibre Assemblies. *Nanotechnology* **2006**, *17* (14). https://doi.org/10.1088/0957-4484/17/14/R01/meta.

(34) Jiang, H.; Hu, Y.; Li, Y.; Zhao, P.; Zhu, K.; Chen, W. A Facile Technique to Prepare Biodegradable Coaxial Electrospun Nanofibers for Controlled Release of Bioactive Agents. *J. Control. Release* **2005**, *108* (2–3), 237–243. https://doi.org/10.1016/j.jconrel.2005.08.006.

(35) Wang, C.; Yan, K. W.; Lin, Y. D.; Hsieh, P. C. H. Biodegradable Core/Shell Fibers by Coaxial Electrospinning: Processing, Fiber Characterization, and Its Application in Sustained Drug Release. *Macromolecules* **2010**, *43* (15), 6389–6397. https://doi.org/10.1021/ma100423x.

(36) Blaiszik, B.; Kramer, S. L. B.; Moore, J. S.; Sottos, N. R.; Blaiszik, B. J.; Kramer, S. L. B.; Olugebefola, S. C.; Moore, J. S.; Sottos, N. R.; White, S. R. Self-Healing Polymers and Composites Second Sandia Fracture Challenge View Project Shock Wave Energy Dissipation by Mechanochemically-Active Materials View Project Self-Healing Polymers and Composites. *Annu. Rev. Mater. Res* **2010**, *40*, 179–211. https://doi.org/10.1146/annurev-matsci-070909-104532.

(37) Hwang, T. H.; Lee, Y. M.; Kong, B. S.; Seo, J. S.; Choi, J. W. Electrospun Core-Shell Fibers for Robust Silicon Nanoparticle-Based Lithium Ion Battery Anodes. *Nano Lett.* **2012**, *12* (2), 802–807. https://doi.org/10.1021/nl203817r.

(38) Zhou, W.; Zhou, K.; Liu, X.; Hu, R.; Liu, H.; Chen, S. Flexible Wire-like All-Carbon Supercapacitors Based on Porous Core-Shell Carbon Fibers. *J. Mater. Chem. A* **2014**, *2* (20), 7250–7255. https://doi.org/10.1039/c3ta15280d.

(39) Wu, X.; Han, Z.; Zheng, X.; Yao, S.; Yang, X.; Zhai, T. Core-Shell Structured Co3O4 @ NiCo2O4 Electrodes Grown on Fl Exible Carbon Fibers with Superior Electrochemical Properties. **2017**, *31* (November 2016), 410–417. https://doi.org/10.1016/j.nanoen.2016.11.035.

(40) Li, X.; Zang, X.; Li, Z.; Li, X.; Li, P.; Sun, P.; Lee, X.; Zhang, R.; Huang, Z.; Wang, K.; Wu, D.; Kang, F.; Zhu, H. Large-Area Flexible Core-Shell Graphene/Porous Carbon Woven Fabric Films for Fiber Supercapacitor

Electrodes. *Adv. Funct. Mater.* **2013**, *23* (38), 4862–4869. https://doi.org/10.1002/adfm.201300464.

(41) Baek, J.; Lee, E.; Lotz, M. K.; D'Lima, D. D. Bioactive Proteins Delivery through Core-Shell Nanofibers for Meniscal Tissue Regeneration. *Nanomedicine Nanotechnology, Biol. Med.* **2019**, *23*, 102090. https://doi.org/10.1016/j.nano.2019.102090.

(42) Hwang, J.; Min, B.; Lee, J. S.; Keem, K.; Cho, K.; Sung, M. Y.; Lee, M. S.; Kim, S. Al 2 O 3 Nanotubes Fabricated by Wet Etching of ZnO/Al 2 O 3 Core/Shell Nanofibers. *Adv. Mater.* **2004**, *16* (5), 422–425. https://doi.org/10.1002/adma.200305209.

(43) Kang, Y. Q.; Cao, M. S.; Yuan, J.; Zhang, L.; Wen, B.; Fang, X. Y. Preparation and Microwave Absorption Properties of Basalt Fiber/Nickel Core-Shell Heterostructures. *J. Alloys Compd.* **2010**, *495* (1), 254–259. https://doi.org/10.1016/j.jallcom.2010.01.143.

(44) Bae, H. S.; Haider, A.; Selim, K. M. K.; Kang, D. Y.; Kim, E. J.; Kang, I. K. Fabrication of Highly Porous PMMA Electrospun Fibers and Their Application in the Removal of Phenol and Iodine. *J. Polym. Res.* **2013**, *20* (7). https://doi.org/10.1007/s10965-013-0158-9.

(45) Shim, J.; Lee, J. S.; Lee, J. H.; Kim, H. J.; Lee, J. C. Gel Polymer Electrolytes Containing Anion-Trapping Boron Moieties for Lithium-Ion Battery Applications. *ACS Appl. Mater. Interfaces* **2016**, *8* (41), 27740–27752. https://doi.org/10.1021/acsami.6b09601.

(46) Fane, A. G.; Wang, R.; Hu, M. X. Synthetic Membranes for Water Purification: Status and Future. *Angew. Chemie - Int. Ed.* **2015**, *54* (11), 3368–3386. https://doi.org/10.1002/anie.201409783.

(47) Lalia, B. S.; Kochkodan, V.; Hashaikeh, R.; Hilal, N. A Review on Membrane Fabrication: Structure, Properties and Performance Relationship. *Desalination* **2013**, *326*, 77–95. https://doi.org/10.1016/j.desal.2013.06.016.

(48) Sukitpaneenit, P.; Chung, T. S. Molecular Elucidation of Morphology and Mechanical Properties of PVDF Hollow Fiber Membranes from Aspects of Phase Inversion, Crystallization and Rheology. *J. Memb. Sci.* **2009**, *340* (1–2), 192–205. https://doi.org/10.1016/j.memsci.2009.05.029.

(49) Nguyen, Q. T.; Alaoui, O. T.; Yang, H.; Mbareck, C. Dry-Cast Process for Synthetic Microporous Membranes: Physico-Chemical Analyses through Morphological Studies. *J. Memb. Sci.* **2010**, *358* (1–2), 13–25.

https://doi.org/10.1016/j.memsci.2010.04.022.

(50) Kim, J. K.; Taki, K.; Ohshima, M. Preparation of a Unique Microporous Structure via Two Step Phase Separation in the Course of Drying a Ternary Polymer Solution. *Langmuir* **2007**, *23* (24), 12397–12405. https://doi.org/10.1021/la7013896.

(51) Zhao, J.; Luo, G.; Wu, J.; Xia, H. Preparation of Microporous Silicone Rubber Membrane with Tunable Pore Size via Solvent Evaporation-Induced Phase Separation. *ACS Appl. Mater. Interfaces* **2013**, *5* (6), 2040–2046. https://doi.org/10.1021/am302929c.

(52) Ghosh, A. K.; Hoek, E. M. V. Impacts of Support Membrane Structure and Chemistry on Polyamide-Polysulfone Interfacial Composite Membranes. *J. Memb. Sci.* **2009**, *336* (1–2), 140–148. https://doi.org/10.1016/j.memsci.2009.03.024.

(53) Dorosti, F.; Omidkhah, M. R.; Pedram, M. Z.; Moghadam, F. Fabrication and Characterization of Polysulfone/Polyimide-Zeolite Mixed Matrix Membrane for Gas Separation. *Chem. Eng. J.* **2011**, *171* (3), 1469–1476. https://doi.org/10.1016/j.cej.2011.05.081.

(54) Freger, V. Nanoscale Heterogeneity of Polyamide Membranes Formed by Interfacial Polymerization. *Langmuir* **2003**, *19* (11), 4791–4797. https://doi.org/10.1021/la020920q.

(55) Zhou, B. W.; Zhang, H. Z.; Xu, Z. L.; Tang, Y. J. Interfacial Polymerization on PES Hollow Fiber Membranes Using Mixed Diamines for Nanofiltration Removal of Salts Containing Oxyanions and Ferric Ions. *Desalination* **2016**, *394*, 176–184. https://doi.org/10.1016/j.desal.2016.05.016.

(56) Apel, P. Track Etching Technique in Membrane Technology. *Radiat. Meas.* **2001**, *34* (1–6), 559–566. https://doi.org/10.1016/S1350-4487(01)00228-1.

(57) Chen, C.; Wang, L.; Huang, Y. Electrospinning of Thermo-Regulating Ultrafine Fibers Based on Polyethylene Glycol/Cellulose Acetate Composite. *Polymer (Guildf).* **2007**, *48* (18), 5202–5207. https://doi.org/10.1016/j.polymer.2007.06.069.

(58) Sill, T. J.; von Recum, H. A. Electrospinning: Applications in Drug Delivery and Tissue Engineering. *Biomaterials* **2008**, *29* (13), 1989–2006. https://doi.org/10.1016/j.biomaterials.2008.01.011.

(59) Li, L.; Jiang, Z.; Li, M.; Li, R.; Fang, T. Hierarchically Structured PMMA Fibers Fabricated by Electrospinning. *RSC Adv.* **2014**, *4* (95), 52973–52985.

https://doi.org/10.1039/c4ra05385k.

(60) Erukhimovich, I.; de la Cruz, M. O. Effect of PVDF Characteristics on Extruded Film Morpholofy and Porous Membranes. **2004**, 1219–1229. https://doi.org/10.1002/polb.

(61) Kurumada, K. I.; Kitamura, T.; Fukumoto, N.; Oshima, M.; Tanigaki, M.; Kanazawa, S. I. Structure Generation in PTFE Porous Membranes Induced by the Uniaxial and Biaxial Stretching Operations. *J. Memb. Sci.* **1998**, *149* (1), 51–57. https://doi.org/10.1016/S0376-7388(98)00179-3.

(62) Kitamura, T.; Kurumada, K. I.; Tanigaki, M.; Ohshima, M.; Kanazawa, S. I. Formation Mechanism of Porous Structure in Polytetrafluoroethylene (PTFE) Porous Membrane through Mechanical Operations. *Polym. Eng. Sci.* **1999**, *39* (11), 2256–2263. https://doi.org/10.1002/pen.11613.

(63) Kondo, A.; Ishigure, T.; Koike, Y. Fabrication Process and Optical Properties of Perdeuterated Graded-Index Polymer Optical Fiber. *J. Light. Technol.* **2005**, *23* (8), 2443–2448.

(64) Lau, W. J.; Ismail, a F. Progress in Interfacial Polymerization Technique on Composite Membrane Preparation. *2nd Int. Conf. Environ. Eng. Appl.* **2011**, *17* (August), 173–177.

(65) Yang, X.; Teng, D.; Liu, B.; Yu, Y.; Yang, X. Nanosized Anatase Titanium Dioxide Loaded Porous Carbon Nanofiber Webs as Anode Materials for Lithium-Ion Batteries. *Electrochem. commun.* **2011**, *13* (10), 1098–1101. https://doi.org/10.1016/j.elecom.2011.07.007.

(66) Lai, J. Y.; Lin, S. F.; Lin, F. C.; Wang, D. M. Construction of Ternary Phase Diagrams in Nonsolvent/Solvent/PMMA Systems. *J. Polym. Sci. Part B Polym. Phys.* **1998**, *36* (4), 607–615. https://doi.org/10.1002/(SICI)1099-0488(199803)36:4<607::AID-POLB7>3.0.CO;2-L.

(67) Witte, P. Van De; Berg, J. W. A. Van Den; Feijen, J. Phase Separation Processes in Polymer Solutions in Relation to Membrane Formation. *J. Memb. Sci.* **1996**, *117*, 1–31. https://doi.org/10.1016/0376-7388(96)00088-9.

(68) McKelvey, S. Phase Separation, Vitrification, and the Manifestation of Macrovoids in Polymeric Asymmetric Membranes. *J. Memb. Sci.* **2003**, *112* (1), 29–39. https://doi.org/10.1016/0376-7388(95)00197-2.

(69) Ziabicki, A. *Fundamentals of Fibre Formation*; Wiley, 1976.

(70) Termonia, Y. Fundamental of Polymer Coagulation. **1995**. https://doi.org/10.1002/polb.1995.090330213.

(71) Kim, S.; Kim, M.; Lim, S. K.; Park, Y. Titania-Coated Plastic Optical Fiber Fabrics for Remote Photocatalytic Degradation of Aqueous Pollutants. *J. Environ. Chem. Eng.* **2017**, *5* (2), 1899–1905. https://doi.org/10.1016/j.jece.2017.03.036.

(72) Vild, A.; Teixeira, S.; Kühn, K.; Cuniberti, G.; Sencadas, V. Orthogonal Experimental Design of Titanium Dioxide - Poly(Methyl Methacrylate) Electrospun Nanocomposite Membranes for Photocatalytic Applications. *J. Environ. Chem. Eng.* **2016**, *4* (3), 3151–3158. https://doi.org/10.1016/j.jece.2016.06.029.

(73) Apetz, R.; Van Bruggen, M. P. B. Transparent Alumina: A Light-Scattering Model. *J. Am. Ceram. Soc.* **2003**, *86* (3), 480–486. https://doi.org/10.1111/j.1151-2916.2003.tb03325.x.

(74) Reddy, K. M.; Manorama, S. V.; Reddy, A. R. Bandgap Studies on Anatase Titanium Dioxide Nanoparticles. *Mater. Chem. Phys.* **2003**, *78* (1), 239–245. https://doi.org/10.1016/S0254-0584(02)00343-7.

(75) Siah, W. R.; Lintang, H. O.; Shamsuddin, M.; Yuliati, L. High Photocatalytic Activity of Mixed Anatase-Rutile Phases on Commercial TiO2 Nanoparticles. *IOP Conf. Ser. Mater. Sci. Eng.* **2016**, *107* (1). https://doi.org/10.1088/1757-899X/107/1/012005.